AGU PUBLICATIONS

JGR

Journal of Geophysical Research: Planets

RESEARCH ARTICLE
10.1002/2013JE004591

Key Points:
- A new DEM of Io has been constructed using Voyager and Galileo stereo pairs
- Global-scale undulations contain implications for Io's heating mechanism
- Topography of recognized and undetected regional-scale features is revealed

Supporting Information:
- Readme
- File S1
- Figure S1
- Figure S2
- Figure S3
- Figure S4
- Figure S5
- Figure S6
- Figure S7
- Figure S8
- Figure S9
- Figure S10
- Figure S11
- Figure S12
- Figure S13
- Figure S14
- Figure S15
- Figure S16
- Figure S17
- Figure S18

Correspondence to:
O. L. White,
oliver.l.white@nasa.gov

Citation:
White, O. L., P. M. Schenk, F. Nimmo, and T. Hoogenboom (2014), A new stereo topographic map of Io: Implications for geology from global to local scales, *J. Geophys. Res. Planets*, *119*, 1276–1301, doi:10.1002/2013JE004591.

Received 12 DEC 2013
Accepted 20 MAY 2014
Accepted article online 24 MAY 2014
Published online 13 JUN 2014

A new stereo topographic map of Io: Implications for geology from global to local scales

Oliver L. White[1], Paul M. Schenk[2], Francis Nimmo[3], and Trudi Hoogenboom[2]

[1]NASA Ames Research Center, Moffett Field, California, USA, [2]Lunar and Planetary Institute, Houston, Texas, USA, [3]Department of Earth and Planetary Sciences, University of California, Santa Cruz, California, USA

Abstract We use Voyager and Galileo stereo pairs to construct the most complete stereo digital elevation model (DEM) of Io assembled to date, controlled using Galileo limb profiles. Given the difficulty of applying these two techniques to Io due to its anomalous surface albedo properties, we have experimented extensively with the relevant procedures in order to generate what we consider to be the most reliable DEMs. Our final stereo DEM covers ~75% of the globe, and we have identified a partial system of longitudinally arranged alternating basins and swells that correlates well to the distribution of mountain and volcano concentrations. We consider the correlation of swells to volcano concentrations and basins to mountain concentrations, to imply a heat flow distribution across Io that is consistent with the asthenospheric tidal heating model of Tackley et al. (2001). The stereo DEM reveals topographic signatures of regional-scale features including Loki Patera, Ra Patera, and the Tvashtar Paterae complex, in addition to previously unrecognized features including an ~1000 km diameter depression and a >2000 km long topographic arc comprising mountainous and layered plains material.

1. Introduction

No instrumentation specifically designed to measure the topography of a planetary surface has ever been deployed to the Galilean moon Io, meaning that alternative techniques using spacecraft imagery must be relied upon. Previous topographic studies of Io have used stereo photogrammetry (3-D) and photoclinometry (2-D shape-from-shading, or "PC") analysis of Voyager and Galileo images to derive digital elevation models (DEMs) of localized areas of geological interest [*Schenk and Bulmer*, 1998; *Schenk et al.*, 1997, 2001, 2004]. Shadow lengths have also been used to obtain the elevations of individual mountains [*Schenk et al.*, 2001]. At a global scale, various studies have used stereographic techniques, Io's gravity field, control point network analyses, and Voyager and Galileo limb profiles to estimate the radii for Io's three ellipsoidal axes [*Davies and Katayama*, 1981; *Synnott et al.*, 1985; *Gaskell and Synnott*, 1987; *Gaskell et al.*, 1988; *Davies et al.*, 1998; *Thomas et al.*, 1998; *Anderson et al.*, 2001; *Oberst and Schuster*, 2004]. Using control points, *Gaskell et al.* [1988] also mapped large swells and basins on regional and global scales.

Despite these measurements of Io's global shape and the topography of select localities, no global stereo DEM of Io has yet been compiled. This is mainly a consequence of Io being the most difficult solar system body to map topographically using stereo analysis, due to the complex and changing photometric behavior and inherent characteristics of the Ionian surface [*Schenk et al.*, 2004]. However, a global topographic map of Io would yield numerous scientific benefits at different scales. Constraining the global-scale, low-amplitude topography of Io is significant as modeling predicts that it may be correlated with the distribution of heat flow across the satellite, which may in turn reveal the primary source of tidally forced heating within its interior [*Peale et al.*, 1979; *Ross and Schubert*, 1985; *Schubert et al.*, 1986; *Segatz et al.*, 1988; *Ross et al.*, 1990; *Tackley*, 2001; *Tackley et al.*, 2001]. *Gaskell et al.* [1988] and *Thomas et al.* [1998] used their respective data sets to derive triaxial figures that best fit the shape of Io; these have, in turn, been used by *Gaskell et al.* [1988], *Ross et al.* [1990], and *Thomas et al.* [1998] to infer Io's mass distribution and heat flow, as well as the extent to which elevations of long-wavelength topography deviate from the idealized figure. Results from these studies were consistent in determining that elevations over areas larger than ~500 km deviate from the figure by no more than ±1 km, but the data used to derive these values are discontinuous, comprising individual limb profiles or widely separated data points in a control network, with interstitial topography being interpolated from these. We present a new stereo DEM of Io that has been mosaicked using all available individual stereo DEMs derived from both Voyager and Galileo imagery, and which has

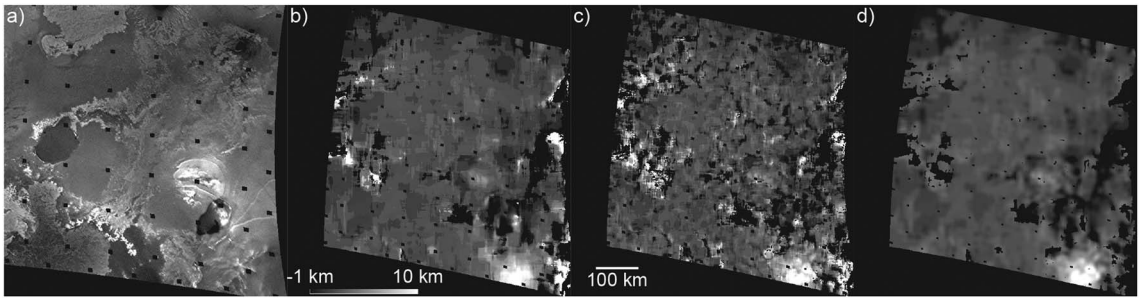

Figure 1. (a) Right-hand image of a stereo pair centered at 4°S, 281°W, reprojected from Voyager image 1639016. The north spur of Boösaule Montes is visible at lower right. North is to the upper right. (b) DEM created from the stereo pair, with a patch size of 31 by 31 pixels. (c) DEM created from the stereo pair, with a patch size of 15 by 15 pixels. The larger patch size in Figure 1b produces an overall smoother DEM with reduced noise levels compared to that in Figure 1c. The abrupt discontinuities in elevation that are apparent in both DEMs tend to reach about 1 km in magnitude. (d) DEM mosaicking the 15 by 15 component in the high-relief areas onto the 31 by 31 component in the plains areas, with a 3 by 3 pixel smoothing filter being applied afterward.

been controlled using Galileo limb profiles. Using both Voyager and Galileo data sets is essential to this venture, as they mostly cover opposite hemispheres of Io, sub-Jovian for Voyager, and anti-Jovian for Galileo; in total, our DEM covers ~75% of the surface. The map represents a continuous topographic data set that will allow us for the first time to precisely identify the amplitudes and lateral extents of long-wavelength variations in Io's topography and correlate them, if possible, with mapped geology [*Williams et al.*, 2011]. In a forthcoming publication, we intend to present an analysis of the topography of paterae and layered plains as measured using photoclinometry DEMs; preliminary results of this study are presented in *White and Schenk* [2014].

2. Stereo Photogrammetry

The only available topographic ground data for Io are in the form of Galileo limb profiles, which were used by *Thomas et al.* [1998] to derive a global shape for Io. Limb profiles can be informative with respect to revealing the long-wavelength topography of the terrain they traverse, as well as localized features of low relief, such as layered plains. However, topographic depressions, such as paterae, are not manifested within limb profiles, and topography of high-relief features that are not actually coincident with the predicted ground track of the limb (which shall be termed "off-limb" features) can corrupt the profiles. In addition, limb profiles provide topographic information for only discrete locations on the surface. Similarly, shadow lengths can be used in a few locations to determine heights (mostly restricted to mountains on Io), yet sufficiently high-resolution data to obtain reliable measurements are scarce. We therefore use stereo photogrammetry to produce regional DEMs of Io's topography. Details of this technique have already been described in *Schenk et al.* [2004], and here we describe how we have modified it to address the ambiguities and sources of error that have afflicted stereo DEMs produced in earlier studies.

Our stereo method is an automated photogrammetry package based on scene-recognition algorithms [*Schenk et al.*, 1997; *Schenk and Bulmer*, 1998], which attempt to match albedo patterns in finite-sized patches in each of the two stereo images, from which parallax and the corresponding difference in elevation can be determined. This technique is confounded by the anomalous photometric characteristics of Io's surface, not least changes resulting from Io's extremely active volcanism, but also the fact that much of it comprises low-contrast, featureless volcanic plains at the 300–2000 m/pixel resolutions typical of the images used in the stereo pairs. Combined with excessive radiation noise and data compression artifacts in many Galileo images, these factors result in most of the stereo DEMs we create exhibiting high levels of noise and data dropouts; in general, stereo DEMs of Io are noisier compared to those created for the other Galilean satellites [e.g., *Schenk*, 2002] as well as the Saturnian icy satellites using Cassini data [e.g., *Moore and Schenk*, 2007; *Bland et al.*, 2012; *Phillips et al.*, 2012; *White et al.*, 2013]. Noise can be removed using standard image noise filters or manually by visual comparison of the stereo pair and DEM, but it has also been found that the presence of noise in a DEM can be changed by varying the patch size used. Larger patch sizes will tend to produce successful matches more often than smaller patches, meaning that using larger patch sizes

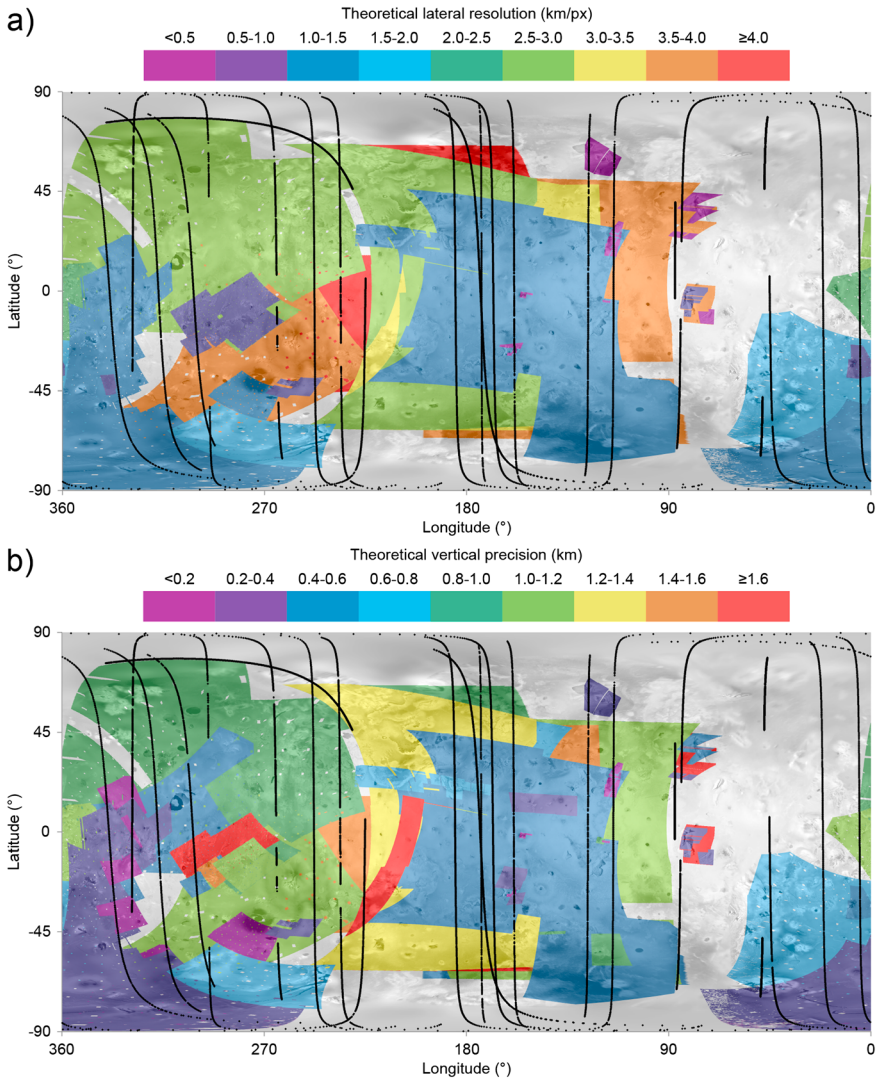

Figure 2. Maps of (a) theoretical stereo DEM resolution and (b) theoretical stereo DEM vertical precision, both overlain on a mosaic of Voyager and Galileo visible imagery. Ground tracks of data used in this study and listed in Table 1 are overlain on both maps. The positions are calculated for the ideal ground tracks; some of the higher peaks may depart slightly from these tracks. Gaps are where limb data were noisy due to plumes, compression effects, low contrast in transit image, or radiation or other photometric effects [*Thomas et al.*, 1998].

generally results in less noise for a given DEM [*Schenk et al.*, 2004]. However, large patch sizes will also produce smoother DEMs in which fine detail is lost compared to when smaller patches are used. This effect is demonstrated in Figure 1. For each stereo pair, we have therefore created two DEMs using two different patch sizes. A larger patch size retains the smoothness of the featureless volcanic plains within the scene and minimizes noise therein, while a smaller patch size resolves detailed features in high-relief terrain such as massifs, which display comparatively little noise in general due to possession of high-albedo contrast and strong parallax. Only the larger patch size is used if no mountainous terrain is identified in the area of stereo overlap. The small patch size DEM may therefore be cropped around any high-relief terrain within it and mosaicked onto the large patch size DEM in order to achieve a single DEM with optimal resolution across all types of terrain. Stereo DEMs in theory attain a lateral resolution equivalent to that of the lowest-resolution image within the stereo pair that is used to create the DEM. The global map in Figure 2a displays the theoretical lateral stereo resolution coverage across Io; Figure 2b displays the theoretical vertical precision coverage of DEMs across Io, calculated based on the lateral resolution and viewing angles of the separate images in each stereo pair.

Table 1. Characteristics of the 24 Galileo Images and Single Voyager Mosaic (Final Row) From Which Limb Topography Has Been Extracted[a]

Image	Number of Points	Longitude at 0° Latitude (°W)	Resolution (km/pixel)	Subspacecraft Position Latitude (°)	Subspacecraft Position Longitude (°W)
349542165	228	339.0	22.79	−3.98	69.0
349542200	227	339.0	22.78	−3.98	69.0
349673952	347	173.8	13.93	−2.74	263.8
349673965	332	173.8	13.93	−2.74	263.8
349674000	352	173.9	13.93	−2.73	263.9
349746313	338	247.8	15.37	−0.35	337.8
349746339	314	247.8	15.37	−0.35	337.8
350013800	447	301.6	8.84	3.51	211.6
350024300	454	317.2	9.89	3.00	227.2
359986578	1386	84.5	4.95	0.63	174.6
374575845	909	225.1	5.90	−0.70	135.1
383600839	474	5.0	10.91	−0.36	95.0
389654039	482	21.3	10.49	−0.43	111.3
389771978	828	185	6.12	−0.48	275.0
389752400	894	168.1	5.74	−0.60	258.1
394519145	405	173.4	10.48	−0.12	263.4
401785378	546	158.8	8.32	0.20	68.8
401863178	683	236.1	6.17	0.33	146.1
420626378	677	114.6	10.43	−0.21	24.7
368641300	768	328.7	4.13	−0.13	238.7
420669000	438	125.9	9.66	−0.16	35.9
506406778	595	47.9	1.30	0.36	137.8
506406839	622	48.1	1.30	0.36	138.1
520821239	776	87.2	1.49	0.10	177.2
1638902/1638910	983	218.1	1.35	−11.81	308.2

[a]Note that the pair 349542165 and 349542200, the pair 349746313 and 349746339, and the trio 349673952, 349673965, and 349674000 each share almost the exact same ground tracks.

Once noise in the separate DEM components has been eliminated, steep elevation gradients can still remain in the data. These artifacts can be especially apparent when large patch sizes are used, whereby in areas with little topographic relief over large lateral scales (i.e., plains), broad zones of near-constant elevation exist (to within a few hundred meters), separated from other zones by sharp (often a few pixels) topographic cutoffs, the relief of which corresponds to the vertical precision of the DEM. To correct this problem, the DEM is processed with a smoothing filter to reduce the magnitude of these discontinuities (Figure 1d). A box size is defined for the filter, and each pixel in the DEM is designated an elevation value equal to the mean elevation of all pixels within a box centered on that particular pixel. Typically, the component of the DEM generated with a large patch size will be processed with a coarser smoothing filter than that used to process the small patch size component, prior to the two components being mosaicked.

3. Control of Stereo DEMs

Each of our stereo DEM products are constructed from framing camera Voyager and Galileo images tied to a global control network and are accurate laterally to within roughly 1 km everywhere on the surface. This digital control network includes at least 95% of all Voyager and Galileo images better than 20 km/pixel resolution and is published by *Schenk* [2010] in the form of global and regional map products. This network is comparable to within a few kilometers of the limb profile network (P. Thomas, personal communication, 2013), and as Ionian topographic features have scant high-frequency topographic detail (such as impact craters), any offset has negligible effect.

Before the stereo DEMs can be globally projected and mosaicked together, they must be controlled in order that they fit the triaxial ellipsoid of Io as defined by the limb profiles [*Thomas et al.*, 1998]. Vertical control of the stereo DEMs is achieved using 25 limb profiles (24 Galileo and 1 Voyager) provided by Peter Thomas, which include an additional 7 to the 18 that *Thomas et al.* [1998] used to determine the global shape of Io. The 25 profiles are composed of 10,441 data points, add up to a total length of 105,180 km, and have a

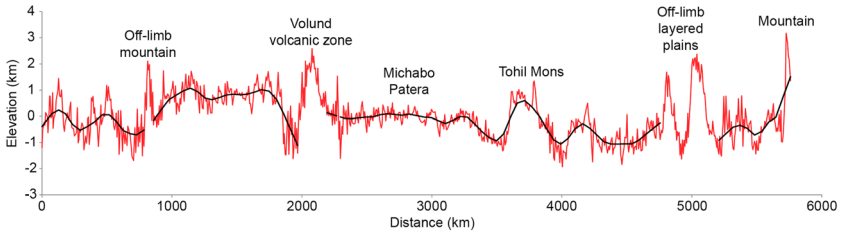

Figure 3. Raw (red line) and smoothed (black line) limb profiles for Galileo image 389752400. North is at the left end of the profile.

mean point spacing of 10.1 km. Table 1 lists the characteristics of the parent images for each of these profiles, the ground tracks of which are mapped in Figure 2. The raw limb profiles, which range in resolution from 1.3 to 22.8 km/pixel, display varying degrees of noise, and so have been smoothed in order to eliminate short-wavelength (tens of kilometers), high-amplitude (several kilometers) noise features. Figure 3 displays the effect of this smoothing for the profile obtained from Galileo image 389752400. In addition to noise, *Thomas et al.* [1998] noted that the most usual systematic error in limb-fitting solutions comes from the limb coordinates being an envelope over high topography rather than an actual topographic profile. However, this effect is minimal on a mostly smooth object such as Io, where the only off-limb influence will really come from randomly distributed high-relief features, such as mountains and layered plains. *Thomas et al.* [1998] calculated that the difference between the limb envelope and profiles at the calculated ground track would introduce fit ellipse errors of less than 50 m, which is far below noise levels in all the profiles. For the purpose of controlling the DEMs, features in the profiles that are interpreted to originate from off-limb sources, which include plume effects as well as topography, are eliminated from the profile before they are used to control the DEMs.

Identification of noise and off-limb features is guided by overlaying the limb profiles on the geological map of *Williams et al.* [2011] and assessing the correlation between prominent topographic features in the limb profiles and mapped geological features (Figure 5b). For a particular stereo DEM to be controlled using these profiles, useable data (i.e., not off-limb data) from two or more limbs must cross the DEM, in order that a plane that describes the difference in topography between that expressed in the DEM and that in the limb profiles can be defined; no plane can be defined if only one limb profile is available. This plane is then used to "tilt" the DEM to make it fit the global reference frame as defined by the limb profiles. This process is illustrated in Figure 4. If two or more limbs do not cross a certain DEM, then that DEM must be controlled by defining an elevation difference plane for it using the topography of other, controlled DEMs that overlap it.

A total of 70 regional- to global-scale DEMs (ranging from 0.14 to 4.08 km/pixel in resolution) has been used to create the global stereo mosaic, 38 created from Voyager stereo pairs, and 32 from Galileo pairs. The lateral resolution map in Figure 2a shows that the highest-resolution coverage comprises Voyager data at the sub-Jovian side of Io (around 330° longitude) and Galileo data at the anti-Jovian side (around 140° longitude). Of the 70 DEMs, 35 have been controlled using the limb profiles and 32 have been controlled using overlapping, controlled DEMs. The three stereo DEMs that cover Hi'iaka and Shamshu Montes, at 75°W, 5°S, are the only ones that cannot be tilted using either coincidental limb profiles or underlying DEMs, and so their elevations have been shifted such that those of the plains areas match those in the nearest limb profiles (Galileo 359986578 and 520821239). A consequence of the inability to control all the DEMs using limb profiles is that after mosaicking the separate DEMs together to form the global map, some topographic mismatching on the scale of >1 km in elevation can remain at certain boundaries between DEMs. Where this situation applies, mismatched topography on either side of the boundary must be masked. In addition, a smoothing filter is applied to the plains areas of the completed global map to further eliminate topographic "seams" between DEMs, as described in section 4 below.

4. Comparison of Stereo and Limb Profile Topography

The fully processed stereo DEM is shown in Figure 5a, overlain on a visible mosaic, and the smoothed limb topography is shown in Figure 5b, overlain on the global geological map of *Williams et al.* [2011]. The

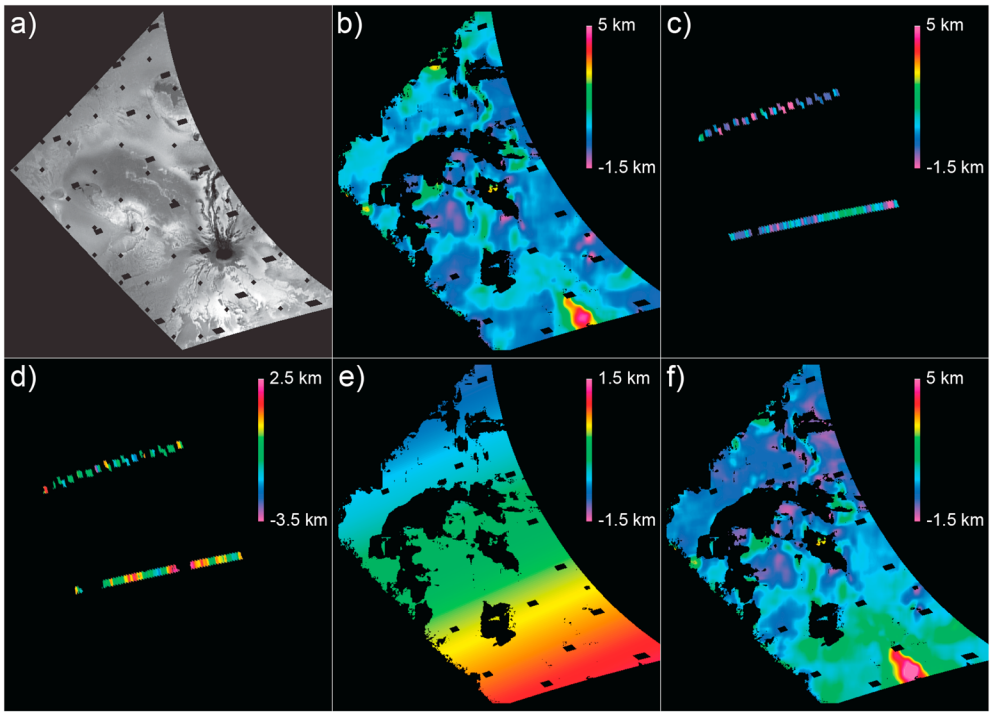

Figure 4. Processing sequence for controlling stereo DEMs using limb profiles. (a) Area of overlap between left and right stereo images (Voyager 1639259 and 1639006), covering Ra Patera. North is to the right. (b) Stereo DEM of the same area that has been processed to remove noise and smoothed. (c) Topography of segments of Galileo limb profiles (349542165/349542200 and 368641300) that traverse the stereo DEM. (d) Map of elevation difference created by subtracting the stereo DEM from the limb topography. (e) The elevation difference map is used to define a plane of elevation difference across the whole area of the stereo DEM that will be used to tilt the DEM in order that it fits the global shape. (f) The final controlled stereo DEM.

stereo DEM is constructed by overlying individual DEMs of higher lateral resolution on those of inferior resolution (as shown in Figure 2a). A broad smoothing filter has been applied to the plains areas in order to remove any remaining noise (on a scale of kilometers in vertical relief and tens of kilometers in lateral extent) that is inconsistent with the appearance of the plains in the visible images. The filter box dimensions measure 199 by 199 pixels, with the dimensions of the entire DEM being 11,500 by 5750 pixels. However, the filter has not been applied to localized topographic features including mountains, layered plains, and some paterae in order to preserve the detailed topographic signatures that they show in the stereo data. The mean elevation of the smoothed stereo DEM is 0.11 km above datum, with a standard deviation of ±0.89 km. The cub file of the DEM is included in the supporting information that accompanies this paper, along with a short guide to the use of this data set.

In order to assess the stereo DEM's quality as a data product, it must be reconciled with the only directly measured relative heights for Io's topography in the form of the limb profiles, specifically by quantifying topographic residuals in profiles with identical ground tracks in the limb and DEM data. The predominantly north–south oriented limb profiles provide excellent latitudinal comparisons of topography but are more problematic for longitudinal comparisons [*Thomas et al.*, 1998]. The supporting information that accompanies this paper compares the limb topography with the DEM topography for the 18 limb profiles where the two data sets overlap; the profiles adopt the same format as those presented in Figure 8. Figure 6 maps the residuals left by subtracting the elevations of the DEM from the limb profiles where the two data sets overlap; Figure 7 is a histogram of the residuals. The mean absolute residual has a magnitude of 0.61 km; 58% of all residual values are negative; 51.6% of all the residuals have a magnitude less than 0.5 km, while 19.5% have a magnitude of 1 km or greater. These more extreme residuals tend to be confined to the edges of limb segments and are generally interpreted to result from short-wavelength noise that was not suppressed by the filter applied to the stereo DEM, or

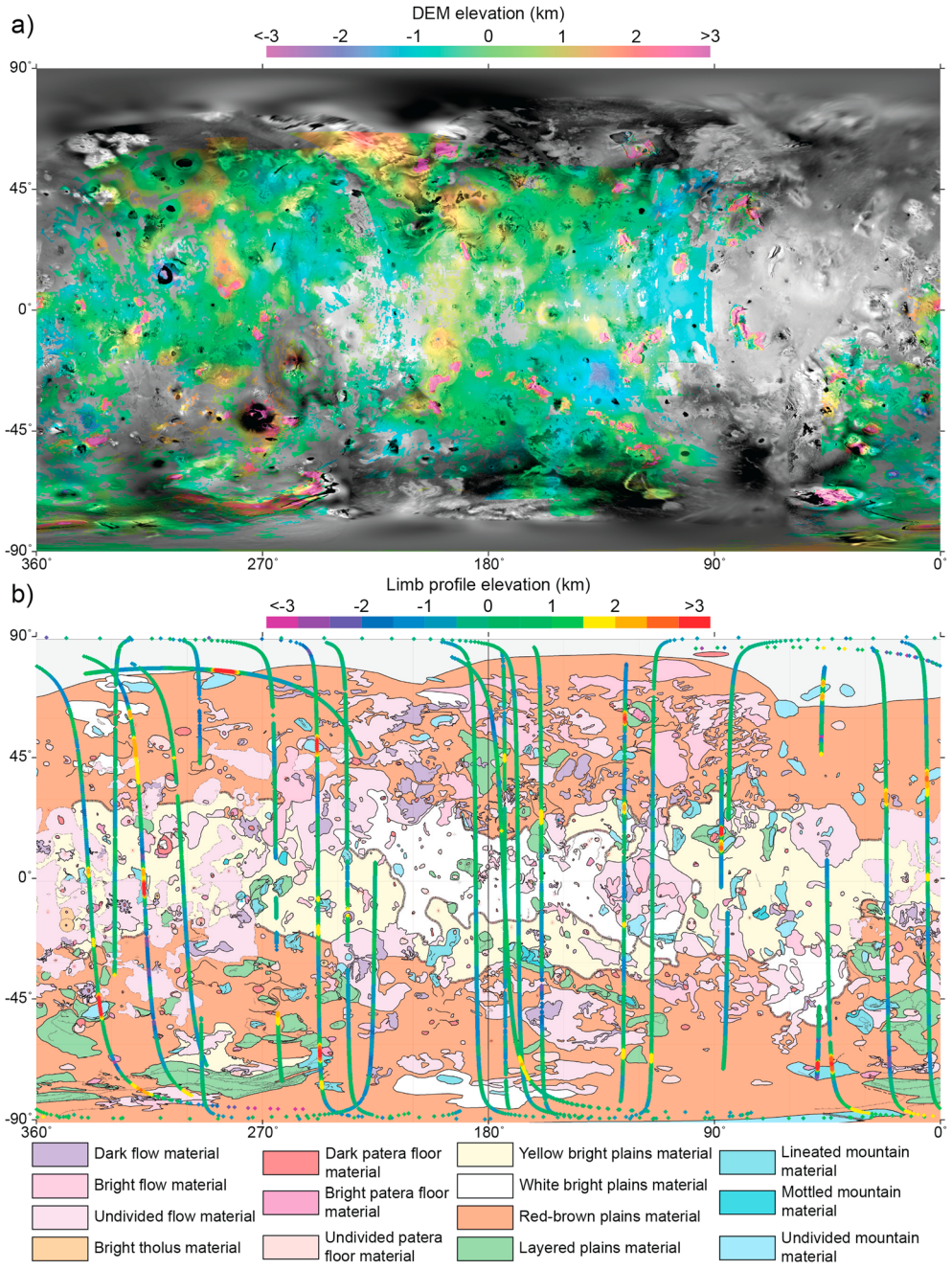

Figure 5. (a) DEM overlain on a mosaic of visible Voyager and Galileo images in simple cylindrical projection at 2 km/pixel. Gaps in the DEM represent masked noise or absence of stereo coverage. A broad smoothing filter has been applied to the plains areas of the DEM post-mosaicking but not to comparatively high relief features such as mountains, layered plains, and some paterae. (b) Limb profiles overlain on a geological map of Io [*Williams et al.*, 2011]. The topography in the profiles has been processed with a smoothing filter to eliminate short-wavelength, high-amplitude noise in the raw data.

from a few instances where the off-limb topography had not been entirely eliminated from the limb profile (e.g., the high positive residual on the north edge of Haemus Montes at 43°W, 66°S). The five profiles with equator-crossing longitudes ranging from 159°W to 185°W display the most consistently low magnitude residuals; these profiles mostly display low noise levels and coincide with a portion of the stereo DEM corresponding to stereo data of fairly high resolution (1.48 km/pixel).

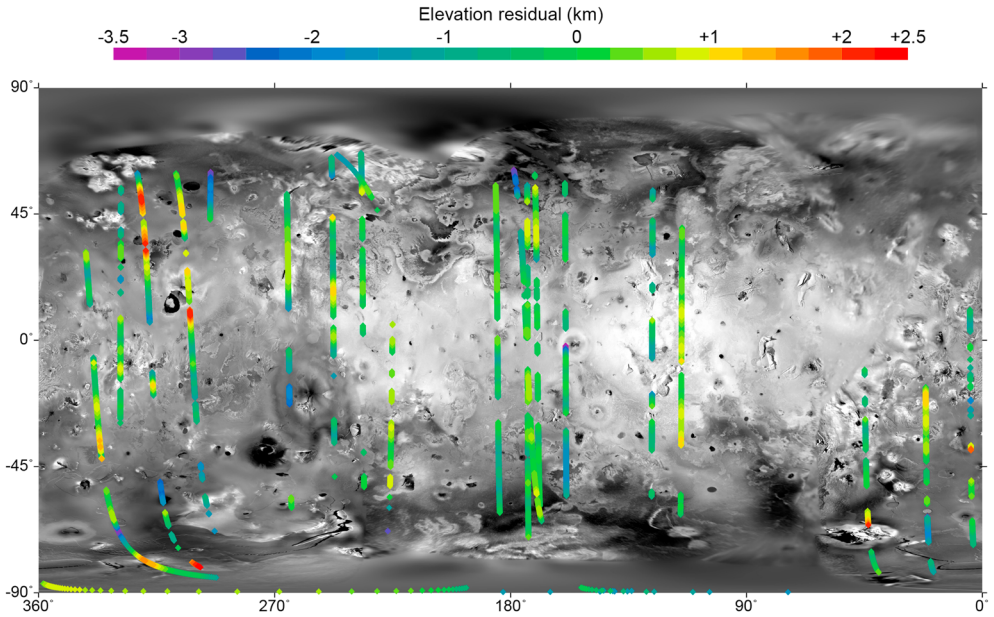

Figure 6. Map of residuals left from subtracting DEM elevations from limb profile elevations where the two data sets overlap, and omitting off-limb segments of the limb profiles. Map overlain on a mosaic of visible Voyager and Galileo images in simple cylindrical projection at 2 km/pixel.

Yet areas of laterally sustained high residuals reaching several hundreds of kilometers across do exist that cannot reasonably derive from either short-wavelength noise or off-limb topography. In these locations, high residuals exist because the limb topography reaches extreme elevations whereas the DEM topography remains fairly level at around 0 km. While it will have some effect, the level DEM topography is not considered to be caused solely by the smoothing filter applied to the stereo DEM, which will not suppress topographic signatures that are on the scale of these residual anomalies, i.e., several hundred kilometers across (see Figure 3). Such residuals are instead interpreted to result from anomalous topography within the limb profiles. If topography of generally consistent elevation within several limb profiles is used to control a DEM, then the resulting controlled DEM will display a best fit to the majority of the topography in the limbs but will stray from any extreme limb topography that exists. Three locations in particular display sustained, high-residual segments: 325.5°W, 74°S (in Galileo 349542165 and 349542200), 158.5°W, 45.5°S (in Galileo 401785378), and 320°W, 41.5°N (in Galileo 350024300). Figure 8 shows the raw and smoothed limb profiles with the sections of overlap in the corresponding DEM profiles for each of the three limb ground tracks that contain these locations. The individual DEMs that coincide with these locations were each controlled using at least three limb profiles, and the latter two locations are coincident with apparent anomalies in the limb data that were described by *Thomas et al.* [1998].

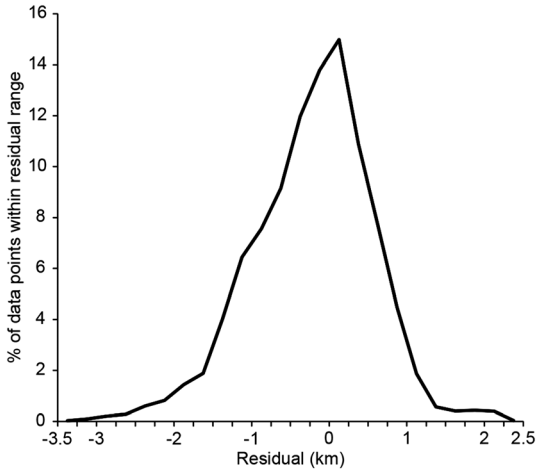

Figure 7. Histogram of residuals between the limb profile and DEM topography, as mapped in Figure 6 (i.e., omitting off-limb segments of the limb profiles). Bin size is 0.25 km.

Limb profiles 349542165 and 349542200, which share the same ground track, display highly undulating terrain at their southern end that varies in elevation between 3.09 km below the DEM and then 2.98 km above it (in the raw limb data), creating a residual range of magnitude 6.07 km stretching across 315 km. These profiles also show similarly highly undulating terrain at their northern ends, yet there is no overlap with the DEM here. Neither of

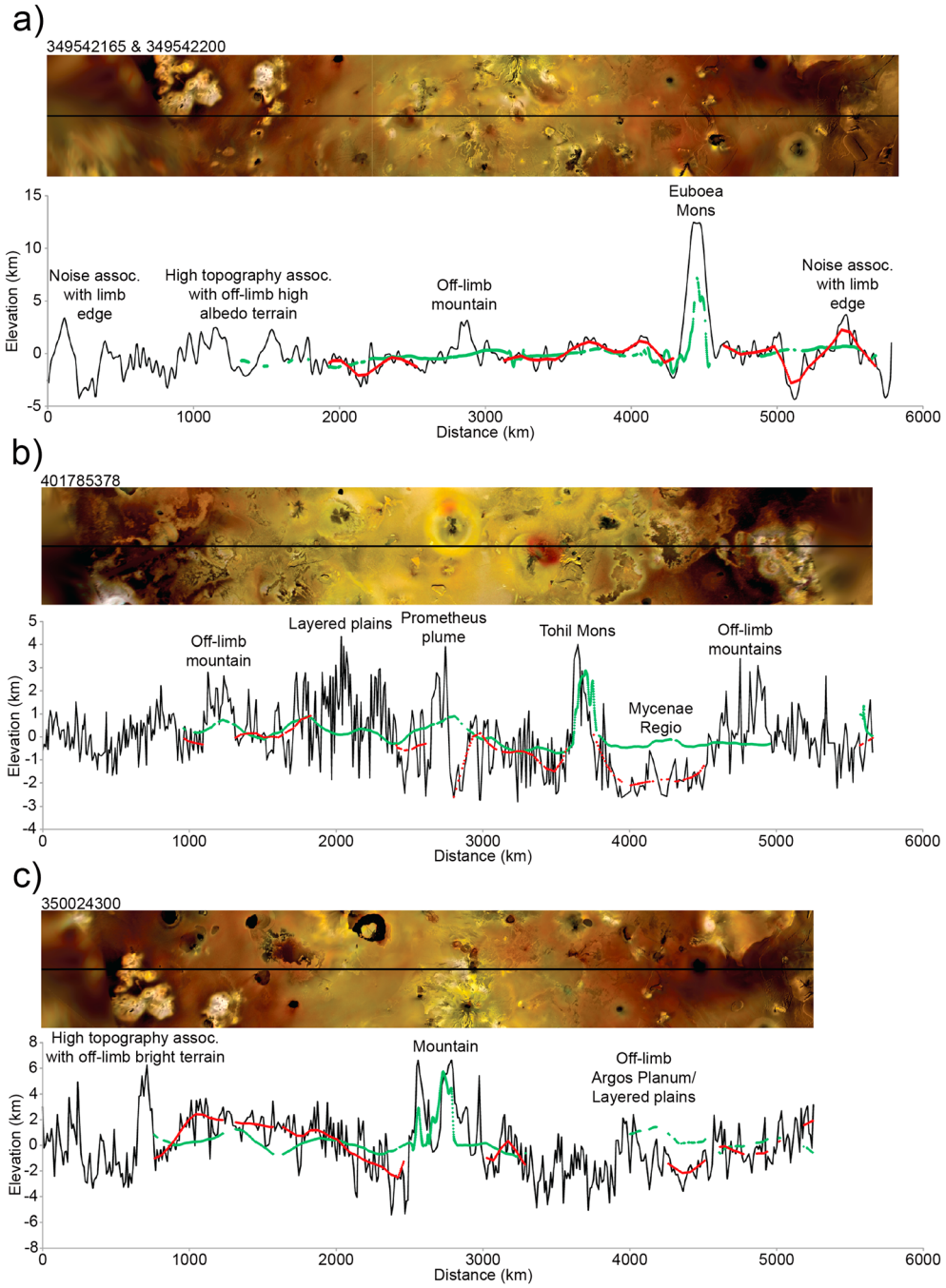

Figure 8. Comparisons of three limb profiles (both raw and smoothed) with profiles from the stereo DEM: (a) Galileo 349542165 and 349542200, (b) Galileo 401785378, and (c) Galileo 350024300. The raw limb profiles are shown in black and the DEM profiles in green. The portions of the smoothed limb profiles that overlap the DEM profile, and which are not considered to be influenced by off-limb topography, are shown in red. Profiles 349542165 and 349542200 share the same ground track, and a mean raw profile is presented. Topographic features that lie on the profile ground tracks, as well as off-limb features that appear in the raw limb topography, are indicated. Ground tracks are shown above the profiles on mosaics of visible Voyager and Galileo images.

these profiles shows especially severe short-wavelength noise, yet the effects of their very low resolution (at 22.8 km/pixel, the lowest amongst all the profiles) and the highly oblique illumination of the limb proximal to the poles (where the contrast between the dimly lit limb and black background will be at a minimum) may combine to produce high inaccuracy in the limb topography at these locations.

At 158.5°W, 45.5°S, profile 401785378 (resolution 8.32 km/pixel) features a fairly level depression of mean elevation −1.90 km (in the raw limb data) that spans 20° of latitude. This feature is not reflected in the DEM, which has a mean elevation of −0.40 km within the same latitude boundaries. *Thomas et al.* [1998] highlighted this feature and considered the magnitude of the depression to be within the short-wavelength noise limits of profile 401785378. However, the 95% confidence limits (2σ) of this segment of the raw profile are ±1.06 km, which does not result in overlap with the mean DEM elevation.

Thomas et al. [1998] also noted that profile 350024300 (resolution 9.89 km/pixel) shows a difference in elevation between northern and southern midlatitudes of about 3 km that is not reflected in profiles in nearby longitudes. This hemispheric dichotomy is not evident in the DEM topography, as shown by the high positive and negative residuals in this profile in Figure 8c (although there is minimal overlap between the two data sets in the southern portion). The northern portion has a mean elevation of 1.45 km over 35° of latitude (in the raw limb data), centered at 38.5°N, with associated 95% confidence limits of ±0.54 km. As with profile 401785378, these short-wavelength noise limits do not result in overlap with the mean DEM elevation of 0.27 km within the same latitude boundaries.

The cause of extreme topography in the aforementioned profiles is enigmatic. While we have noted the possibility that the high residuals in profiles 349542165 and 349542200 are a result of their position near the edge of the limb and the low resolution of the profiles, in general, there is no clear relationship between the resolution of a limb profile and its mean absolute residual. An alternative explanation may be that the anomalous topography is a consequence of compression effects in the Galileo images from which the limb profiles are extracted. *Thomas et al.* [1998] described how the raw limb profiles that we have used in this study have been processed to remove obvious short-wavelength, high-amplitude compression artifacts, but there is the possibility that the regional- and global-scale undulations that do not correlate with the topography in neighboring profiles may represent subtler manifestations of compression effects.

5. The Global Shape of Io

5.1. Global-Scale Topography in the Stereo DEM

The final DEM covers around 75% of Io's total surface area, with the largest gaps in coverage existing at all longitudes north of 65°N, at all latitudes between 45°W and 90°W, and north of the equator between longitudes 350°W and 90°W. Outside of these areas, however, there is sufficiently continuous coverage to allow definition of subtle variations in Io's shape to an extent that was not possible for the control point and limb studies of *Gaskell et al.* [1988] and *Thomas et al.* [1998].

Gaskell et al. [1988] claimed to identify a longitudinal arrangement of broad, alternating basins and swells in the altimetry map produced using their Voyager control point network, with high regions at ~90° spacing, and with most elevations over areas larger than ~500 km (~16° arc) in diameter deviating from the triaxial figure by no more than ±1 km. The largest swell was located in Media Regio, centered near the equator at 70°W, with ~2 km relief. However, the uncertainties in the depths of the basins and heights of the swells were more than half their amplitudes. Based on examination of the limb profiles, *Thomas et al.* [1998] deduced similarly minimal global-scale topography, with topography over distances of more than 800 km (25° arc) not exceeding 2 km, but could not confirm the longitudinally arranged swells and basins of the amplitude suggested by *Gaskell et al.* [1988]. The shape parameters of the Galileo control point network study of *Oberst and Schuster* [2004] were in good agreement with those from previous studies of Galileo images and gravitational data [*Davies et al.*, 1998; *Thomas et al.*, 1998; *Anderson et al.*, 2001], but differed significantly from those of the Voyager control point network of *Gaskell et al.* [1988], and had insufficient accuracy to resolve any long-wavelength, global-scale topography.

The long-wavelength topographic variation of Io can be quantified from the global stereo DEM by removing topography associated with localized, high-relief topographic features (including mountains, layered plains, and some paterae), such that only the smoothed relief in the interstitial plains areas between −2 and +2 km in elevation remains (which accounts for 97.6% of the entire DEM). Figure 9 presents a histogram for the elevation within the plains areas of the stereo DEM. With the high-relief terrain removed, the global mean elevation is 0.00 km, with a standard deviation of ±0.61 km, and 89.9% of the elevation values for the plains areas are within ±1 km elevation, indicating minimal topographic variation across Io that is

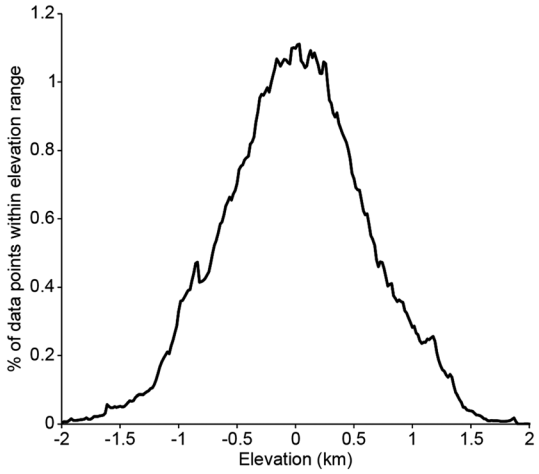

Figure 9. Elevation histogram for the plains portion of stereo DEM, i.e., disregarding elevations below −2 km and above +2 km for high-relief topographic features such as paterae, layered plains, and mountains.

consistent with the magnitude of variation as determined by the control point network and limb profile studies of *Gaskell et al.* [1988] and *Thomas et al.* [1998], respectively. However, neither the 90° spacing of longitudinal basins and swells that were reported in *Gaskell et al.* [1988] nor the dichotomy between moderately high topography in the north polar region and the nearly neutral topography in the south polar region as described by *Ross et al.* [1990] seems to be evident in our stereo DEM. This may partly be a consequence of the incomplete global coverage of the DEM (notably in the north polar region), but the features presented in the global maps of *Gaskell et al.* [1988] and *Ross et al.* [1990] are absent from parts of the DEM with consistent coverage across broad spans of longitude. In this sense, our DEM is consistent with the findings of *Thomas et al.* [1998], which also could not confirm these features and

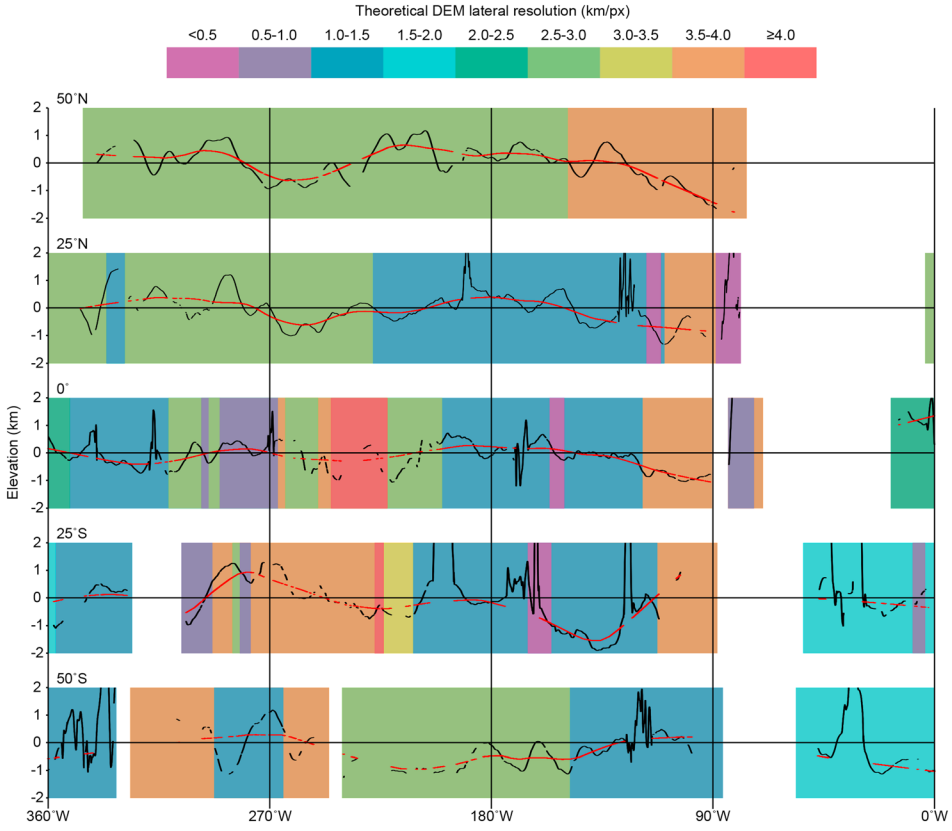

Figure 10. Latitudinal profiles drawn across 360° of longitude on the stereo DEM at five latitudes. Black profiles represent the original profiles drawn across the DEM and red profiles have been processed using a broad smoothing filter. Elevation scales extend from −2 to +2 km in all cases; 0° profile measures 11,444 km long, 25° profiles measure 10,371 km long, and 50° profiles measure 7356 km long. Colors overlain on the profiles represent the theoretical lateral resolution of the individual DEMs that contributed to the stereo DEM, as indicated in the scale bar above the profiles.

Table 2. Statistics of the Locations and Mean Elevations of the Basins and Swells[a]

Basin/Swell	Basin/Swell Longitudinal Boundaries (°W)	Basin/Swell Center Longitude (°W)	No. of DEM Data Points Within Basin/Swell ($\times 10^6$)	Mean Elevation in DEM (km)	Mean Elevation of Spherical Harmonics Topography Within Basin/Swell (km)	Center Longitude of Corresponding Mountain/Volcano Concentration (°W)	Spatial Density of Mountains Within Basin/Swell		Spatial Density of Volcanoes Within Basin/Swell	
							$l = 2$ to $l = 4$ [*Kirchoff et al.*, 2011]	$l = 3$ to $l = 4$	$l = 2$ to $l = 6$ [*Kirchoff et al.*, 2011]	$l = 3$ to $l = 6$
Basin 1	[81.1] to 140.8	[110.9]	3.62	−0.47 (±1.10)	0.02 (±0.14)	65	0.079 (±0.310)	−0.015 (±0.153)	0.024 (±0.147)	−0.004 (±0.167)
Swell 1	140.8 to 208.5	174.6	5.24	0.17 (±0.99)	0.01 (±0.15)	165	−0.145 (±0.153)	0.008 (±0.152)	0.138 (±0.201)	0.002 (±0.127)
Basin 2	208.5 to 273.0	244.7	3.68	−0.13 (±1.01)	0.03 (±0.17)	265	−0.025 (±0.215)	−0.003 (±0.088)	−0.023 (±0.116)	0.002 (±0.112)
Swell 2	273.0 to [345.5]	[310.6]	4.88	0.12 (±1.04)	−0.01 (±0.15)	325	−0.060 (±0.148)	−0.005 (±0.058)	0.040 (±0.295)	0.018 (±0.181)

[a]Identified within the stereo DEM and the corresponding areas in the spherical harmonics topography and the mountain and volcano spatial distribution maps generated by *Kirchoff et al.* [2011] and generated by this study for a scenario that omits the $l = 2$ component from each. Values in straight parentheses indicate those longitude values that are limited by incomplete global coverage in the stereo map. Values in curved parentheses are 95% (2σ) confidence limits. The spatial density units for mountains and volcanoes are arbitrary, with negative and positive values representing densities below and above the global mean, respectively. All basins and swells extend from 32.2°S to 53.3°N in latitude, as defined by the latitudinal limits in stereo DEM coverage.

were also based on limb profile topography, while those of *Gaskell et al.* [1988] and *Ross et al.* [1990] were based on a control point network.

Five latitudinal topographic profiles extending across 360° of longitude have been drawn across the complete stereo DEM to aid with identification any global-scale longitudinal patterns in the topography. The profiles are drawn at 50°S, 25°S, 0°N, 25°N, and 50°N and are shown in black in Figure 10; in order to accentuate global-scale topographic variations on the order of thousands of kilometers in size, the DEM profiles have been processed with a broad smoothing filter, with the resulting profiles shown in red. The profiles tend to be continuous where they traverse portions of the stereo DEM that originate from high-resolution, low-noise stereo data; where lower quality stereo data are traversed, data dropouts are more common. The 0°N, 25°N, and 50°N profiles appear to indicate an arrangement of broad swells and basins, with ~65° of longitude separating low points from high points, and with amplitude of 1 to 1.5 km. While the configuration is not as apparent in the 25°S profile due to less widespread stereo coverage here, as well as perhaps being masked by regional-scale geologic "noise" such as the depression at 25°S, 135°W, we are confident that the basin-swell system can be identified as far south as 32°S in the DEM and as far north as 53°N (essentially the northern limit of stereo coverage). The locations and extents of these swells and basins are described in Table 2 and are highlighted on the DEM of long-wavelength stereo topography in Figure 11a. The mean elevations of the areas within the basins and swells as shown in Table 2 confirm the alternating high-low pattern seen in the profiles. The significance of these basins and swells with respect to correlation to the spatial distribution of volcanoes and mountains, and implications for global heating of Io, will be discussed in section 6.

5.2. Spherical Harmonics of Limb Profile Topography

As an alternative means of deriving global topography using the limb profiles that may be compared with the topography apparent in our DEM, we have expressed the topography in the limb profiles as a summation of spherical harmonic coefficients, in a manner akin to that applied to the Saturnian satellites in *Nimmo et al.* [2011]. *Ross et al.* [1990] performed similar spherical harmonics analysis based on the control point network of *Gaskell et al.* [1988]. Only a summary of the

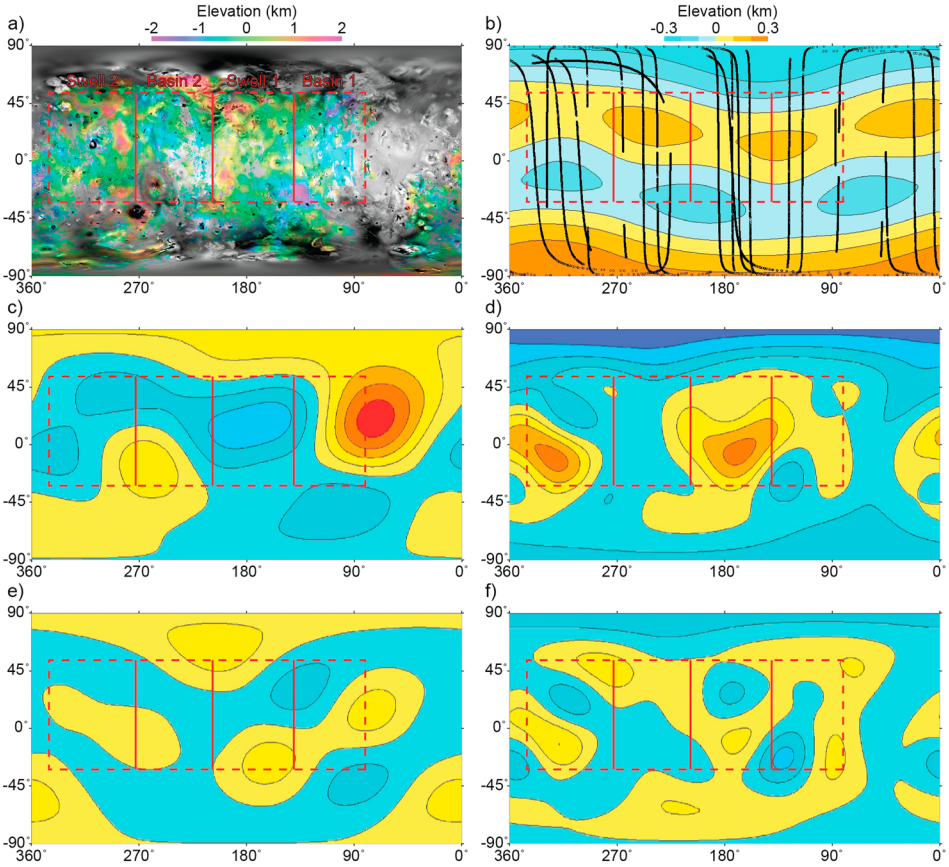

Figure 11. (a) Stereo DEM showing long-wavelength topography between −2 and +2 km elevation. (b) Long-wavelength topography derived from spherical harmonics analysis of the limb profiles using equation 1 with $r = 1 \times 10^6$ and expanded only at the $l = 3$ degree, with the locations of limb profiles indicated in black. Map of the spatial distribution of (c) mountains (expanded from $l = 2$ to $l = 4$) and (d) volcanoes (expanded from $l = 2$ to $l = 6$), reproduced from *Kirchoff et al.* [2011]. Map of the spatial distribution of (e) mountains (expanded from $l = 3$ to $l = 4$) and (f) volcanoes (expanded from $l = 3$ to $l = 6$) that omit the $l = 2$ component. For all six maps, the boundaries of the basins and swells as identified in the stereo DEM are indicated by straight red lines (the boundaries between basins and swells) and dashed red lines (the uncertain outer boundaries of the basins and swells, limited by stereo coverage). In Figures 11c–11f, hot colors (red) indicate more dense concentrations and cool colors (blue) indicate relatively less dense concentrations. In Figures 11c and 11d, the mountain density ranges from 0.3 to 7.4 per 10^6 km^2, with a mean of 2.8 per 10^6 km^2, and the volcano density from 1.8 to 29.3 per 10^6 km^2, with a mean of 13 per 10^6 km^2 [*Kirchoff et al.*, 2011]. Statistics relating to the basins and swells in all six maps are collated in Table 2.

techniques involved is provided here; the reader is directed to *Nimmo et al.* [2011] for a detailed description. The topography, h, of the limb profiles may be expressed as follows:

$$h(\theta, \phi) = R_0 \sum_{l=2}^{N} \sum_{m=0}^{l} \overline{P}_{l,m}[\cos\theta]\left(\overline{C}_{lm} \cos m\phi + \overline{S}_{lm} \sin m\phi\right) \quad (1)$$

where θ is colatitude, ϕ is longitude, R_0 is Io's mean radius, $\overline{S}_{lm}$ and $\overline{C}_{lm}$ are the normalized spherical harmonic coefficients of degree l and order m, and $\overline{P}_{l,m}[\cos\theta]$ are normalized associated Legendre polynomials. The topographic variance at each degree, V_l, is given by

$$V_l = \sum_{m=0}^{l} \overline{C}_{lm}^2 + \overline{S}_{lm}^2 \quad (2)$$

We follow *Nimmo et al.* [2011] by using the limb profile observations to estimate $\overline{S}_{lm}$ and $\overline{C}_{lm}$, subject to an a priori constraint that the 2-D variance spectrum has a spectral slope of −1. This approach ensures that short-wavelength features, which would otherwise cause problems in data gap areas, are attenuated. The

strength of this a priori constraint is given by a dimensionless parameter r [*Bills and Ferrari*, 1977]. Large values of r result in low-amplitude topography, while small values of r result in unrealistic topography in data gap areas [*Nimmo et al.*, 2010]. The optimum value of r is obtained by using synthetic data sets [*Nimmo et al.*, 2011] and is expected to be of the order R_0^2/σ_0^2 (=1.7×10^6), where σ_0^2 is the total topographic variance [*Nimmo et al.*, 2010].

Io's limb profile topography is referenced to a triaxial ellipsoid [*Thomas et al.*, 1998], so the lowest degree for which topography can be estimated is $l = 3$. As far as can be determined using the available coverage of our DEM, the wavelength of the undulations apparent in Figure 11a extends across ~130° longitude, equivalent to a spectral degree of $l \approx 3$ according to the relationship wavelength, $L = (2\pi R_0)/l$. For the purposes of comparison with spherical harmonics topography, and because there are a few large data gaps, we only take the expansion out to $l = 3$, and based on synthetic studies, we take a value of r of 1×10^6. Figure 11b shows the resulting spherical harmonic topography using only an expansion for $l = 3$. The topographic amplitude is much lower in the spherical harmonics topography (extending across a range of 0.5 km) than that in the stereo DEM (which extends across a range of ~4 km), and the topography differs from that in the DEM in that variations appear to be primarily latitude dependent, with lows and highs in opposite hemispheres being antisymmetric about the equator, rather than longitude dependent and symmetrical about the equator as seen in the DEM. The swells and basins identified in the stereo DEM are not evident in the spherical harmonics topography, as indicated in Table 2, which presents mean elevations for the areas of the spherical harmonics topography that correspond to the basins and swells observed in the stereo DEM. The spherical harmonics topography in these locations is actually anticorrelated to the basins and swells in the stereo DEM, but the minimal longitudinal variation of the spherical harmonics topography diminishes the significance of this—the amplitude of the topography only reaches 0.04 km across the area covered by the basins and swells, compared with 0.64 km in the stereo DEM. Lack of stereo coverage at latitudes greater than 65° means that the southern high and northern low in the spherical harmonics topography cannot be confirmed in the DEM. The extent to which the topographic patterns that appear in the stereo DEM correlate to the distributions of mountains and volcanic centers at different spectral degrees is discussed in the next section.

6. Correlation of Topography With Volcano and Mountain Distribution and Heat Flow

Various studies have examined the distribution of volcanoes and mountains across the surface of Io and assessed whether they are related in any way [*Carr et al.*, 1998; *Lopes-Gautier et al.*, 1999; *McEwen et al.*, 1998, 2000a; *Radebaugh et al.*, 2001; *Schenk et al.*, 2001; *Tackley et al.*, 2001; *Kirchoff et al.*, 2011; *Veeder et al.*, 2011, 2012; *Hamilton et al.*, 2013]. Here we will assess the extent to which the long-wavelength topography in our stereo DEM can be correlated to the distribution of volcanoes and mountains as identified by previous studies and to assess the significance of this correlation (or lack of it) with respect to constraining heating models for Io. *Kirchoff et al.* [2011], expanding on the work of *Schenk et al.* [2001], were the first study to specifically and rigorously assess the statistical character and significance of the distributions of both volcanoes and mountains on Io using spherical harmonic analysis and confirmed previous findings that significant latitudinal and longitudinal concentrations exist in the global distribution of mountains and volcanic centers. At the $l = 2$ spectral degree, two broad concentrations in mountain distribution are centered at 25°N, 65°W and 20°S, 265°W (roughly antipodal to each other), as well as two broad concentrations in volcanic center distribution at 5°N, 165°W and 10°S, 325°W (also roughly antipodal to each other). *Hamilton et al.* [2013], focusing specifically on volcanic centers, also identified bimodal peaks in patera distribution between 150°W to 180°W and 330°W to 360°W, with the centers of these peaks being within a few tens of degrees of the maximum concentrations of paterae as identified by *Radebaugh et al.* [2001], *Schenk et al.* [2001], *Kirchoff et al.* [2011], and *Veeder et al.* [2011]. An important caveat when assessing the significance of spatial distribution studies is the effect of spatial variations in image resolution [see *Hamilton et al.*, 2013, Figure 3]; the number of volcanic centers in the region from 30°W to 90°W may be slightly underestimated due to resolution limitations here. Both volcanoes and mountains have been found to concentrate toward the equator, and this skew is likely to be genuine given that image resolution is generally robust between 90°S and 60°N (i.e., mean resolution of 3 km/pixel or better within these latitude boundaries), although it decreases to >4 km/pixel north of 60°N. The regions of highest density of mountains and volcanic centers are

globally anticorrelated, being offset by 90°, and the regions of enhanced volcanic center density are nearly aligned with the tidal axis running from Jupiter through the center of Io. The approximate centers of enhanced distribution for volcanic centers and mountains are offset between 5° and 35° east of the *a* and *b* axes of Io, respectively [*Schenk et al.*, 2001].

The pattern of alternating basins and swells that are apparent in our stereo DEM is also longitudinally arranged and appears to correlate reasonably well to the bimodal and anticorrelated global distribution pattern of mountains and volcanic centers as presented in *Schenk et al.* [2001], *Kirchoff et al.* [2011], and *Hamilton et al.* [2013]. Table 2 presents the spatial density of mountains and volcanoes (as shown in Figure 3 of *Kirchoff et al.* [2011], expanded from $l = 2$ to $l = 4$ for mountains and $l = 2$ to $l = 6$ for volcanoes) within the boundaries of each of the basins and swells identified in the stereo DEM (see Figure 11). Without exception, higher mountain densities are seen to correlate to the basins and lower mountain densities to the swells, while higher volcano densities are seen to correlate to the swells and lower volcano densities to the basins; this association can also be seen in Figures 11c and 11d, which overlays the boundaries of the basins and swells on the maps of *Kirchoff et al.* [2011]. It should be noted that "high" and "low" densities are relative to each landform: The global mean volcano density is higher than that for mountains. The precise locations and extents of the basins/swells and mountain/volcano concentrations correlate to differing degrees. The central longitudes of swell 1 and basin 2 differ from those of their corresponding volcano and mountain concentrations by 10° and 20°, respectively. Regarding latitude, the volcano and mountain concentrations in *Kirchoff et al.* [2011] tend to be centered within 10° of the equator and extend to the midlatitudes, with the exception of the mountain concentration at 90°W, which is centered at ~25°N.

However, at this point, it is important to recall that the wavelength of the basins and swells in the stereo DEM (as far as can be determined using available stereo coverage) covers ~130° of longitude, equivalent to a spectral degree of $l \approx 3$. This represents a higher spectral degree than that ($l = 2$) for which an especially significant anticorrelation was found in the distribution of volcanoes and mountains by *Kirchoff et al.* [2011] and which was considered to implicate models of asthenospheric tidal heating, which is dominated by the $l = 2$ component. Given that Io's limb profile topography is referenced to a triaxial ellipsoid [*Thomas et al.*, 1998], there should not exist any $l = 2$ signature in either our stereo DEM or spherical harmonics topography. In Figures 11e and 11f, we compare the global volcano and mountain distributions as shown in *Kirchoff et al.* [2011] with the resulting distributions that are obtained when the $l = 2$ component is omitted, but including the $l = 3$ and $l = 4$ components for mountain distributions and the $l = 3$ to $l = 6$ components for volcano distributions. The bimodal, anticorrelated pattern of volcanoes and mountains that was apparent in *Kirchoff et al.* [2011] changes to a configuration that features smaller wavelength, lower amplitude highs and lows in spatial distribution that are not as obviously anticorrelated with one another as when the $l = 2$ component was included. Consequentially, there also appears to be little correlation (or anticorrelation) between the high- and low-density zones and the basins and swells of the stereo DEM. Table 2 includes the spatial density of mountains and volcanoes within each of the stereo DEM basins and swells for the scenario where the $l = 2$ component is omitted from the spherical harmonics presented by *Kirchoff et al.* [2011]. The correlation of the alternating high- and low-density zones to the basins and swells of the stereo DEM, which was apparent when the $l = 2$ component was included, is now absent.

Therefore, while the topography and mountain/volcano distributions as presented in Figure 11 show that the basins and swells in the stereo DEM appear to correlate reasonably well to the mountain and volcano spherical harmonics distributions from *Kirchoff et al.* [2011] when the $l = 2$ component is included, but not when it is omitted, they cannot in principle be compared with the mountain and volcano distributions that incorporate the $l = 2$ component due to the DEM being controlled by the limb profiles that are referenced to a triaxial ellipsoid. At the $l = 3$ spectral degree, which is the scale that the wavelength of the basins and swells in the stereo DEM corresponds to, *Kirchoff et al.* [2011] found that very little spectral power is present for the distribution of both volcanoes and mountains and that for what power there is, negligible correlation or anticorrelation exists between the distributions of the two landforms.

The findings of the spherical harmonics investigation of *Kirchoff et al.* [2011] would therefore seem to downplay the significance of the basins and swells in the DEM with respect to correlation of topography to mountain and volcano distributions. However, it should be noted that the basins and swells correlate not only to the *Kirchoff et al.* [2011] $l = 2$ distributions but also to the mountain and volcano distributions as determined by *Schenk et al.* [2001] using counting circles and the volcano distributions as determined by

Hamilton et al. [2013] using nearest-neighbor statistics and distance-based clustering. Therefore, while the stereo DEM basins and swells may not be representative of the $l = 2$ component that is manifested in the volcano and mountain distributions of *Kirchoff et al.* [2011], they do appear to correlate to volcano and mountain distributions derived through these independent methods. Concerning the study of *Veeder et al.* [2012], which quantified the magnitude and distribution of the heat flow from 240 active or recently active volcanic features during the Galileo epoch, we find that bounding longitudes of swell 2 correlate well to a longitudinal zone of high thermal emission [*Veeder et al.*, 2012, Figure 10], even disregarding Loki Patera's disproportionally large contribution, and that basin 2 correlates well to a zone of low emission. However, swell 1 and basin 1 are anticorrelated to longitudinal zones that display low and high thermal emissions, respectively. These correlations and anticorrelations may not be especially significant as the record of thermal emission during the Galileo era will not necessarily be the same as the long-term emission record that accounts for the varying concentrations of volcanic features across Io. Despite their heterogeneous distribution, volcanic centers on Io are sufficiently ubiquitous across its surface such that even areas with "low" volcano concentrations may still display high thermal emission, depending on which volcanic centers happen to be active at the time.

Despite the incomplete stereo coverage, we consider the correlation between the volcano/mountain concentrations that have been observed by several studies and the basins/swells in our DEM to be significant with respect to refining scenarios for global heating on Io. The issues of how heat is transferred from Io's interior to its surface, and of the location of the primary source of the tidal heating, have been the subject of extensive study since the Voyager missions and are considered to be instrumental in governing the distribution of mountains and volcanoes [*Peale et al.*, 1979; *Ross and Schubert*, 1985; *Schubert et al.*, 1986; *Segatz et al.*, 1988; *Gaskell et al.*, 1988; *Ross et al.*, 1990; *Schenk et al.*, 2001; *Tackley*, 2001; *Tackley et al.*, 2001; *Khurana et al.*, 2011; *Hamilton et al.*, 2013]. Amongst various working hypotheses to explain the anticorrelated volcano and mountain concentrations, *Schenk et al.* [2001] considered the most plausible scenario to involve a second global stress mechanism acting to offset the global crustal compressive stress field induced by volcanic subsidence that is regarded to be responsible for mountain formation [*Schenk and Bulmer*, 1998], thereby leading to enhanced volcanism and decreased mountain building in some areas. Stress mechanisms that might potentially fill this role include mantle or asthenospheric convection and nonsynchronous rotation.

Modeling of convection in Io's interior by *Tackley et al.* [2001] indicates that the location of tidal heating strongly influences internal dynamics and heat flow distribution, with asthenospheric heating producing equatorially enhanced, longitudinally varying surface heat flow that is more compatible with the observed bimodal pattern for volcano and mountain building than that produced by mantle heating, where the variation is primarily latitude dependent. Specifically, the asthenospheric heating scenario predicts increased heat flow along the tidal axis (i.e., the sub-Jovian and anti-Jovian points at 0°W and 180°W), coincident with the volcanic concentrations, and decreased heat flow at the leading and trailing points on Io (90°W and 270°W), coincident with the mountain concentrations. The increased heat flow at the sub-Jovian and anti-Jovian points may convert the basal lithosphere into lower density asthenosphere (if they are sufficiently coupled), resulting in isostatic uplift [*Gaskell et al.*, 1988], with outward flow of the rising material leading to crustal or lithospheric thinning and stretching [*Schenk et al.*, 2001]. This would act to reduce the lateral compressional stresses imposed by global subsidence which dominate at Io's leading and trailing points, encouraging volcanism and discouraging mountain building.

By analogy with Europa, the nonsynchronous rotation scenario [e.g., *Greenberg and Weidenshilling*, 1984; *Milazzo et al.*, 2001] involves two large antipodal areas of compressive stress offset 90° from two similar areas of extensional stress. In combination with the high stress levels expected for global subsidence, this scenario would operate in a manner similar to that described for internal convection [*Schenk et al.*, 2001]. In addition, these areas would be displaced to the east of the tidal axis by an amount determined by the rotation history of Io's crust and could match the observed 5° to 35° eastward offsets of mountain and volcano concentrations [*Radebaugh et al.*, 2001; *Schenk et al.*, 2001; *Kirchoff et al.*, 2011].

We consider the correlation of the basin/swell configuration in our DEM to that of the mountain/volcano concentrations as identified by earlier studies to be essentially consistent with the asthenospheric convection scenario. The coincidence of the swells with volcano concentrations supports the hypothesis that these areas are experiencing upwelling of asthenospheric material, creating a net extensional stress that promotes enhanced volcanism. This offsetting extensional stress will be reduced, if not absent, in the areas with lower

surface heat flow where the basins coincide with mountain concentrations, and compressional stresses associated with burial, subsidence, and compression of volcanic deposits predominate [*Schenk and Bulmer*, 1998]. Whereas the upwelling associated with the asthenospheric convection scenario would be expected to create relative differences in elevation between areas of extension and compression, the nonsynchronous rotation scenario requires that there be no large permanent mass asymmetries in Io's crust [*Schenk et al.*, 2001] (and therefore no large density asymmetries) and so does not specifically predict any elevation difference between the separate areas. While the nonsynchronous rotation scenario does represent a possible explanation for the eastward offset of volcanoes/swells and mountains/basins from predicted surface heat flow maxima and minima, respectively, *Hamilton et al.* [2013] discussed various alternatives to nonsynchronous rotation as a means for accounting for this offset. These include lateral migration of upwelling magma toward regions that are more favorable for magmatic ascent, such as existing fault distributions in the lithosphere, but which are not directly correlated with sites of maximum heat production. However, while this may account for the offset of the volcanoes and swells, it does not also explain the offset of the mountains and basins. Another alternative explanation offered by *Hamilton et al.* [2013] is that if the asthenospheric heating produces a global partial melt layer as proposed by *Khurana et al.* [2011], then tides generated within this melt could produce thermal energy that would modify patterns of expected heat flux.

7. Topographic Signatures of Regional-Scale Geological Features in the Stereo Data

A geological map published by *Williams et al.* [2011] represents the most thorough survey of Io's geology to date and was compiled using four colored and monochrome global mosaics created from Galileo and Voyager imagery. The information contained within our DEM comprises an important additional database with which to define geological units and recognize potentially significant relationships between topographic features on Io's surface. The maps in Figure 5 incorporate the various relevant data sets, including the global visible mosaic and the stereo DEM in Figure 5a and the limb topography and the geological map of *Williams et al.* [2011] in Figure 5b, and they permit a thorough investigation of how both the short- and long-wavelength topographies of Io correlate to the mapped geology. Mountains, layered plains, and some paterae are essentially the only units that display characteristic topographic signatures that are resolved in either the DEM or limb topography, while regional-scale plains units do not show distinct topographic signatures. This section will examine the topography of various prominent, large-scale (several hundred to thousands of kilometers) geological features as revealed in the global stereo DEM.

7.1. Depression at 25°S, 135°W

This topographic feature stands out in that it is the most well defined of any regional-scale topographic aberration in the stereo DEM. Figure 12 shows the location of the depression in the DEM and in the geological map of *Williams et al.* [2011], and two topographic profiles plotted across it. It comprises an ~1000 km diameter basin that reaches a nadir of 2 km below the surrounding terrain, which is at an elevation of ~0 km. The depression is punctuated by mountains in its peripheral regions. The extent of the depression is covered in its entirety by stereo data corresponding to a single stereo pair of fairly high theoretical resolution (1.5 km/pixel). No limb profiles pass directly over the depression. In *Williams et al.* [2011], the nadir at the center of the depression is mapped as a unit of "undivided flow material," defined as "smooth lobate flows, typically with intermediate relative albedo and a range of colors… difficult to distinguish individual flow units and to trace flows to source vent(s)." The undivided flow material unit occurs in many other locations across Io that are not associated with depressions, so it is not characterized by an intrinsically negative topographic signature. Instead, the flow material in this instance has likely filled a preexisting topographic depression; the margins of the unit correspond to an approximate contour of −1.5 km elevation, and it is bounded by deposits from an unnamed patera to the west, white plains material to the north, a mountain to the east, and yellow plains material to the south. Two possible sources exist for the flow material: Either it has originated from a vent(s) at the base of the depression that is now completely covered by the flows, which spread radially outward from the vent, or it originated from a vent on the edge of the depression (likely Tupan Patera to the northwest or the unnamed patera to the west at 26°S, 146°W, which both border the flow material), and flowed downgradient. The origin of the depression itself is enigmatic, but if the source

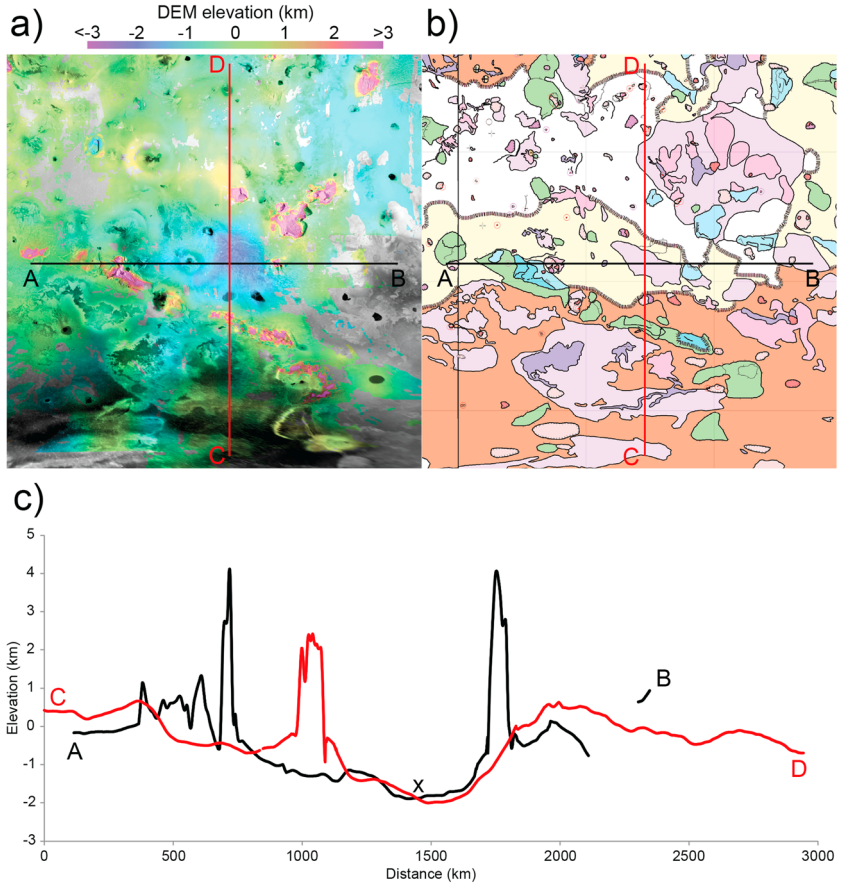

Figure 12. (a) Detail of the stereo DEM containing the depression at 25°S, 135°W. Ground tracks of profiles in Figure 12c are indicated. (b) Portion of the global geological map of *Williams et al.* [2011] covering the same area as that in Figure 12a. Unit classification is the same as that in Figure 5. (c) Topographic profiles across the depression. The cross marks the crossing point of the two profiles.

vent for the flows were to be located at its base, then a volcanic origin that involves subsidence of the surrounding region would represent a possibility.

7.2. Topographic "Arc" at 42.5°S, 169.5°W

High-relief topography on Io is not normally observed to describe regional-scale patterns that may indicate a related origin for the constituent topographic features. A potential exception is a chain of high-relief topography extending from 35°S, 200°W to 55°S, 110°W. The chain is ~2200 km long and is fairly straight in its central portion, curving sharply toward the south at the ends to form an arc-like configuration. As mapped by *Williams et al.* [2011], the chain incorporates mountains and layered plains including Rata, Dorian and Tohil Montes, and Telegonus Mensae. The curve at the western end is formed by the separate mountain units of Dorian and Rata Montes, while the curve at the eastern end is formed by the layered plains unit of Telegonus Mensae and possibly also another layered plains unit to the south that is not resolved in the DEM. The entire chain is covered by stereo data corresponding to a single stereo pair of fairly high theoretical resolution (1.5 km/pixel), although most of Tohil Mons (one of Io's most geologically complex mountains) is covered by higher lateral resolution data reaching 0.2 km/pixel (see Figure 2a). Figure 13 shows the location of the arc in the DEM and in the geological map of *Williams et al.* [2011].

Of the mountainous elements, Dorian Montes and Tohil Mons appear to display a lineated fabric that is aligned parallel both to their crests and to the path of the arc (Figure 13c). The morphologies of these mountains have been described in previous studies [e.g., *Schenk et al.*, 2001; *Turtle et al.*, 2001; *Williams et al.*, 2004]. *Schenk et al.* [2001] described Dorian Montes as consisting of a broadly arching plateau with a

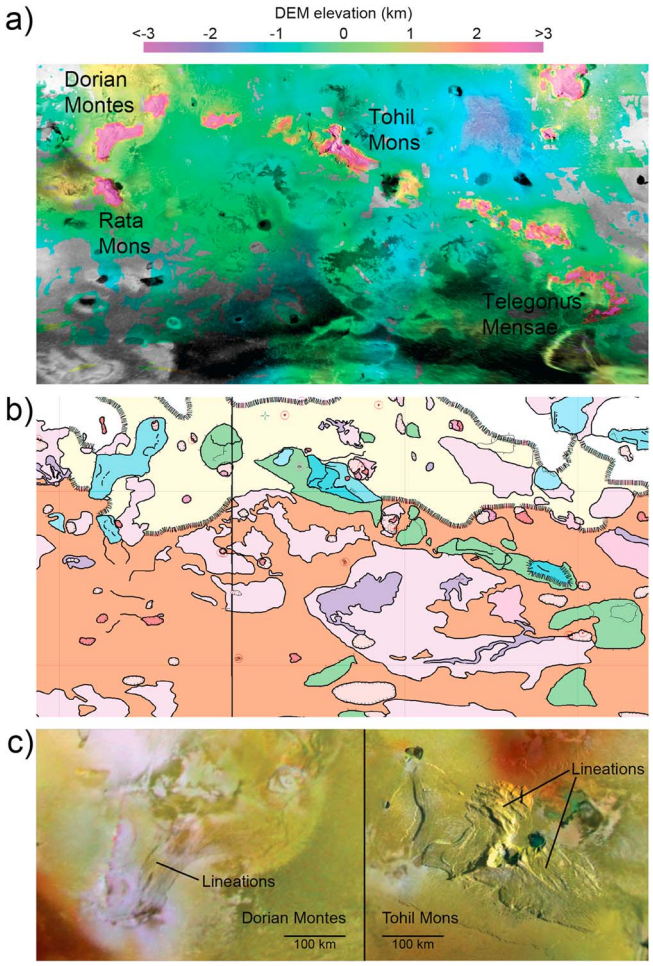

Figure 13. (a) Detail of the stereo DEM containing the topographic "arc" at 42.5°S, 169.5°W. Locations of mountains and layered plains are indicated. (b) Portion of the global geological map of *Williams et al.* [2011] covering the same area as that in Figure 13a. Unit classification is the same as that in Figure 5—mountain units are in light blue, layered plains units are in light green. (c) Details of Dorian and Tohil Montes in Galileo color imagery, highlighting the lineated fabric of these mountains.

striated surface and Tohil Mons as an elongate lineated plateau. The lineations at Dorian Montes are not as well resolved as those at Tohil Montes. *Williams et al.* [2004] distinguished two distinct units of lineated mountain material at Tohil Mons which trend parallel to each other, with the northwest part of the edifice displaying deeper, more pronounced ridges and scarps compared to the more subdued lineations in the northeastern part. *Williams et al.* [2004] interpreted the lineated mountain material to represent faults involved in uplift and/or lateral collapse of the edifice and suggested that formation of Tohil Mons occurred through combination of compressional uplift and surficial extension along the crest. This is consistent with the hypothesis that most mountains on Io are thrust blocks formed by compressive stresses accumulated in the lower crust due to global subsidence of buried volcanic layers [*Schenk and Bulmer*, 1998; *Schenk et al.*, 2001]. Given that the crest-parallel lineations of Dorian and Tohil Montes likely reflect the orientation of the compressive stresses that originally uplifted the mountains, their parallel alignment with the arc may potentially indicate a shared compressive regime that formed both these mountains as well as the others on the arc.

Yet it is important to note that the arc is composed not just of constructional elements (mountains) but also erosional elements (layered plains) and that the arc as a whole may in fact owe more to erosion of preexisting topography than it does to mountain uplift resulting from a compressive regime in this region of Io. Interstitial to the mountains are layered plains units that, for Tohil Mons and the unnamed mountain at 44°S, 125°W, can also surround the mountains and, in these cases, underlie them (see the map unit correlation in *Williams et al.* [2004]). Layered plains are flat-topped, sometimes terraced, plateaus with scalloped margins that show scarp heights of typically <1 km, and which have been attributed to erosion of crustal layers [*Moore et al.*, 2001], or possibly mass wasting of mountains for examples with especially high topography [*Williams et al.*, 2011]. The distribution of the layered plains indicates that the remnants of the preexisting plains unit were preferentially preserved in the present configuration, proximal and interstitial to the mountains. The erosional processes that undermine the plains material, which are currently thought to involve sapping by pressurized, liquid SO_2 in combination with gravity-driven slumping and other mass-wasting processes [e.g., *McCauley et al.*, 1979; *Moore et al.*, 2001; *Davies*, 2007], would presumably initiate in the exposed plains regions, with the retreating erosional scarps isolating the layered plains units around the mountains that overlie them. Due to their comparatively high elevations (>2 km) in the stereo data, there is the possibility that some of the isolated outcrops of layered plains in the arc (e.g., Telegonus Mensae and that at 22°S, 182°W) may actually represent eroded mountainous material rather than

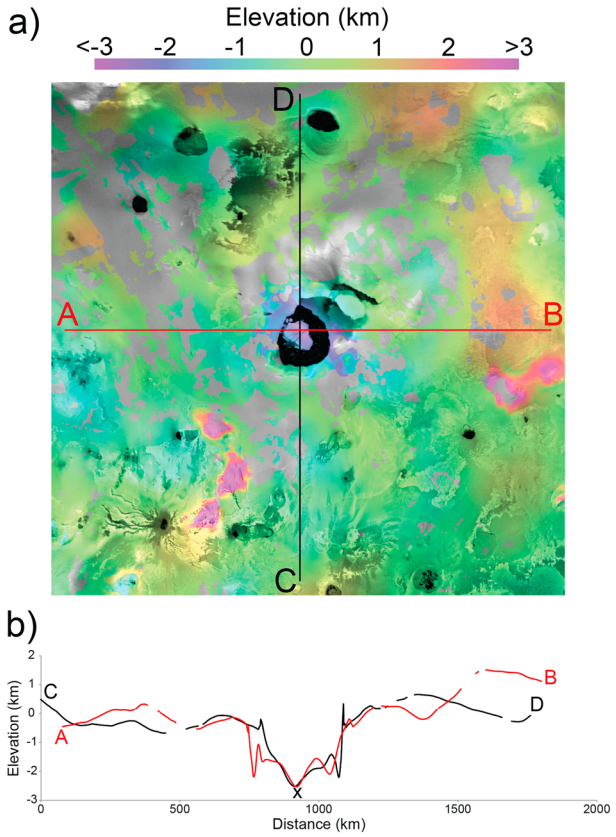

Figure 14. (a) Detail of the stereo DEM containing Loki Patera at 12°N, 310°W. Ground tracks of profiles in Figure 14b are indicated. (b) Topographic profiles across Loki Patera. The cross marks the crossing point of the two profiles.

eroded plains material [*Williams et al.*, 2011]. This would enhance the case for the arc representing the product of a single orogeny that uplifted all the topography contained within it. Otherwise, while the arc-aligned lineations of Dorian and Tohil Montes may suggest a shared formation episode for the mountains, there is the alternative possibility that their formation is unrelated and that the existence of the arc is purely a consequence of the isolation of layered plains units surrounding and interstitial to the mountains.

7.3. Loki Patera

Located at 12°N, 310°W, Loki Patera is Io's largest and most powerful volcano. It appears as a low-albedo, subcircular feature more than 200 km in diameter. What appears to be a fractured "island" takes up ~25% of the area of the patera and is interpreted to be either a resurgent dome or a foundered mountain block [*Davies*, 2007]. The appearance of Loki Patera changed between Voyagers 1 and 2 [*Smith et al.*, 1979] but changed very little between Voyager 1 and the arrival of Galileo. Volcanism at Loki Patera is dominated by silicate magma, and its thermal output can vary between ~10% and 25% of Io's total thermal emission [*Veeder et al.*, 1994]. Resurfacing is currently thought to occur via episodic overturn of a crust covering a lava lake, rather than emplacement of new flows [*Rathbun et al.*, 2002; *Davies*, 2003; *Matson et al.*, 2006; *Howell and Lopes*, 2007].

Loki Patera is covered by three separate stereo pairs, each of theoretical lateral resolution 2.9 km/pixel. Given this relatively low resolution, and the existence of featureless terrain both interior and exterior to the patera, the region is afflicted with considerable noise. However, all three stereo pairs show that Loki Patera is marked by a depression reaching 2 km below the surrounding terrain. Figure 14 shows Loki Patera in the DEM and two topographic profiles plotted across it. The region of low topography is not confined to within the low-albedo interior of the patera; the featurelessness of the terrains that characterize the central island, the patera floor, and the surrounding terrain means that the stereo program relies on the albedo contrast boundaries between the bright island and dark patera floor, and the dark patera floor and the bright surrounding terrain, to determine parallax and associated elevation. When considered alongside the relatively low resolution of the data, the lateral extent of the low topography as shown in the DEM may therefore not necessarily be an especially accurate representation of its true expanse. Unfortunately, no limb profile passes directly over Loki Patera itself or the associated topographic low.

Determining if the topographic low is confined to within the boundaries of Loki Patera, or extends to the surrounding terrain, is dependent on whether a scarp at the rim of the patera can be identified. Based on one of the highest-resolution images acquired of Loki Patera (Galileo 625566413 at 1.1 km/pixel), which was obtained near-terminator, shadow measurements performed by *Turtle et al.* [2004] determined that the rim of the patera cannot be higher than 100 m. In addition, this same Galileo image indicates that the surface of the low-albedo material covering the floor of Loki Patera displays specular reflectance at low Sun angles,

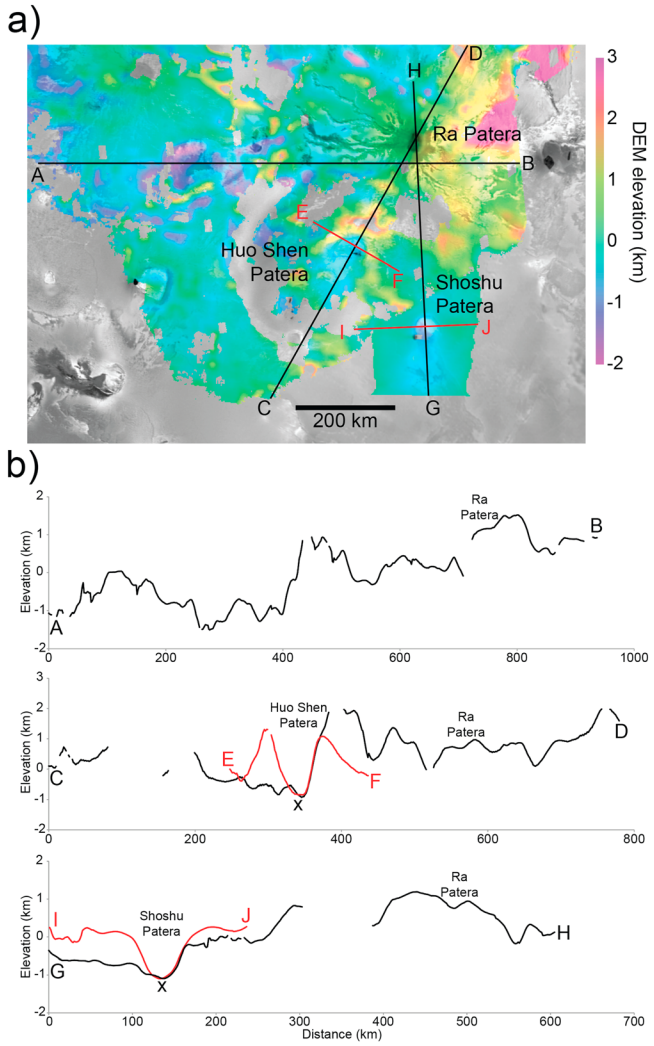

Figure 15. (a) Detail of the stereo DEM containing Ra Patera at 8.5°S, 324.5°W, merged with a PC DEM of Shoshu Patera. Ground tracks of profiles in Figure 15b are indicated. (b) Topographic profiles across Ra Patera, Huo Shen Patera, and Shoshu Patera. The cross marks the crossing points of the Huo Shen and Shoshu profile pairs.

indicative of a very smooth and flat, and possibly glassy, patera floor [*Geissler et al.*, 2004; *Turtle et al.*, 2004; *Matson et al.*, 2006]. The stereo topography displays undulations of several hundred meters across the floor of Loki Patera and cannot resolve the central island, but the 2 km magnitude of the depression associated with the patera and its immediate vicinity is considerably higher than the 100 m rim height estimated by *Turtle et al.* [2004] and suggests that Loki Patera is situated within a broader, deeper depression than its visible rim would imply, the boundaries of which cannot be precisely constrained in the stereo DEM. Geological activity associated with Loki Patera does appear to have extended into the surrounding region at some point in its history—geological units bordering the northeast and southwest of Loki Patera have been mapped as undivided flow material and bright flow material respectively by *Williams et al.* [2011] and show triangulate planforms comparable with that of the present-day, dark-floored (and therefore presumable more recently active) Loki Patera. If these flanking flow units do represent manifestations of earlier patera lava-lake activity, then they may also reside within the regional low indicated in the stereo data.

7.4. Ra Patera

Ra Patera is the largest of Io's radiating, shield-like lava flow fields and, in 1996, was observed by Galileo to be the source of an active plume in addition to a large dark deposit interpreted to be a massive lava flow [*Belton et al.*, 1996]. A geological and stereo topography mapping study of Ra Patera performed by *Schenk et al.* [1997] determined that the summit of Ra Patera rises ~1 km above the surrounding plains, with pre-Voyager-era lava flows occurring on slopes of 0.1° to 0.3°. In our stereo DEM, Ra Patera also shows a positive topographic signature (Figure 15) of ~400 km radius that exhibits similar relief above the surrounding plains to that determined by *Schenk et al.* [1997], with the eastern margin of Ra Patera bounded by a mountain unit reaching 7–8 km high. The topography in the limb profile for Galileo image 368641300, the ground track of which passes 4° (130 km) to the west of the summit of Ra Patera, also indicates a relief of ~1 km. Furthermore, there is indirect evidence for the lateral extent of the topographic high associated with Ra Patera in the form of patera morphologies to the south, as indicated in Voyager imagery as well as stereo and PC topography; 75 km diameter Huo Shen Patera is located 240 km to the southwest of Ra Patera, and 50 km diameter Shoshu Patera is located 350 km to the south. Both of these paterae show complete rims on their north, west, and east sides, but the rims appear to be absent on their south sides, with lava flows originating from the paterae extending hundreds of kilometers south. The flow originating from Huo Shen Patera was mapped by

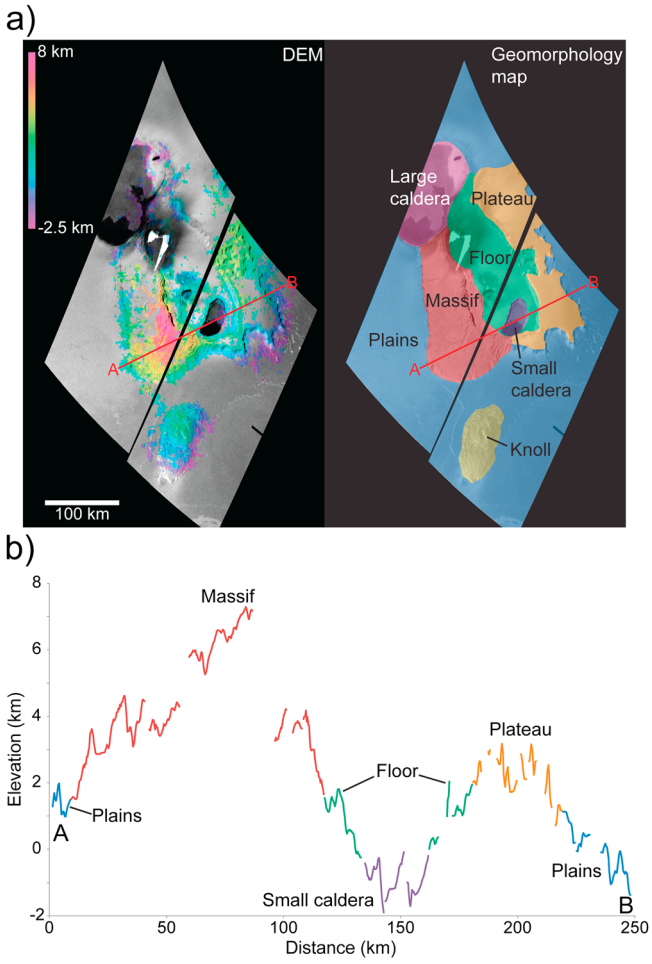

Figure 16. (a) Stereo DEM and geomorphological map of Tvashtar Paterae, both overlain on visible Galileo imagery and with the ground track of the profile in Figure 16b indicated. Bright feature at center is saturation of the Galileo image caused by intense thermal emission from the lava-fountaining episode that was observed in November 1999. (b) Topographic profile taken across Tvashtar Paterae, with the locations of the geomorphological units in the right-hand map of Figure 16a highlighted.

Williams et al. [2011] and appears to be brighter and shorter (~120 km long) than that originating from Shoshu Patera (~210 km long).

These features that are visible in Voyager imagery are reflected in the topography. Figure 15 shows the stereo topography covering Ra Patera and Huo Shen Patera. Shoshu Patera has no stereo coverage, and a PC DEM of Shoshu has been overlain on the stereo DEM (creation and processing of PC DEMs will be described in detail in a forthcoming publication). For both Huo Shen Patera and Shoshu Patera, the topography indicates raised rims on the north, east, and west sides of the paterae, but not on the south rims (Figure 15b), mirroring the Voyager observations. The floor of Shoshu Patera exists at a depth of 1.3 km below the plains that bound it to the north, east, and west. The rim of Huo Shen Patera is raised by as much as 2 km above the patera floor as well as the surrounding plains. The topographic profiles in Figure 15b indicate that zones of low topography that exist roughly at the same level as the respective paterae floors extend southward from the absent south rims, coincident with the lava flows seen in the imagery, and providing further evidence that these flows have breached the south rims of the paterae. For both paterae, the orientations of the flows and their corresponding low-topography zones are aligned directly away from Ra Patera (Figure 15a). When considered with the absent south rims of the paterae, these observations are interpreted to mean that Huo Shen and Shoshu Paterae formed on the southward facing slope of the preexisting Ra Patera topographic high, which was built up by successive lava flows erupted from the patera at the summit of the rise [*Schenk et al.*, 1997]. Lavas erupted from Huo Shen and Shoshu Paterae would have traveled downslope, breaching their respective south rims, and flowing to the south. These observations therefore constrain the lateral extent of the topographic rise associated with Ra Patera by revealing its influence on post-Ra volcanic landforms in the vicinity. Given that Shoshu Patera is located 350 km to the south of Ra Patera, this lateral zone of influence is in good agreement with the approximate radius of the Ra Patera rise as determined from the stereo DEM (400 km).

7.5. Tvashtar Paterae

Tvashtar Paterae comprises a nested caldera complex located at 62°N, 122°W that was the source of a fissure lava-fountain episode observed by Galileo in November 1999 [*McEwen et al.*, 2000b; *Keszthelyi et al.*, 2001; *Wilson and Head*, 2001] and a 330 km high plume observed by New Horizons in February 2007 [*Spencer et al.*, 2007]. Tvashtar Paterae is covered by some of the highest-quality Galileo stereo data to cover a

Table 3. Mean Elevation Values for Each of the Seven Geomorphological Units of the Tvashtar Paterae Complex Identified in Figure 16a[a]

Unit	Massif	Knoll	Mesa	Plains	Floor	Large Caldera	Small Caldera
Mean elevation (km)	4.01 (±3.60)	0.74 (±2.30)	2.14 (±2.01)	0.14 (±2.46)	0.93 (±2.03)	−1.58 (±1.25)	−1.04 (±1.06)
Max. elevation (km)	7.44	2.93	-	-	-	-	-

[a]Maximum elevation values are provided for the "high elevation" units that include the massif and knoll and reflect the summit elevations attained by these features. Values in parentheses are 95% (2σ) confidence limits.

volcanic complex on Io, with a theoretical lateral resolution of 0.3 km/pixel, and which are able to resolve the different elevations of the different components of the complex, although the lack of surface albedo contrast for many of the units means that much of their stereo data is noisy and has to be masked. Figure 16a shows the stereo DEM of Tvashtar Paterae alongside a map that highlights the main geomorphological units of the complex, both overlain on Galileo imagery. Figure 16b shows a topographic profile drawn across the stereo DEM that highlights the locations of different units and provides an indication of their relative elevations. Despite the fact that many of these units appear to show flat surfaces in the Galileo imagery, with adjacent units separated by steep scarps, the profile indicates that in the stereo data the units tend to show steep gradients across their lateral extents, with little indication of scarps separating units. This is a consequence of the minimal surface albedo contrast shown by many of the units, meaning that the stereo program can often only obtain reliable elevation measurements at the well-defined scarp boundaries between units, which paradoxically represent locations where the elevation changes between units. The topographic expressions of the units therefore tend to represent lower or upper portions of the gradients across these scarp boundaries as inferred by the stereo program.

However, reliable measurements for the elevations of each of the units have been derived from the stereo data by drawing 10 topographic profiles across the DEM. Table 3 presents elevation measurements for each of the seven units based on these profiles. Elevation measurements for each unit are shown in Table 3 and include maximum values for the "high elevation" units of the massif and the knoll, for which reliable summit elevations can be obtained due to the high parallax and surface relief shown by these units. Based on these measurements, the floors of the small and large calderas of the complex are 2.0 and 1.7 km below the level of the surrounding terrain, respectively (the illumination angles of the available images of Tvashtar Paterae are such that these values cannot be compared with those from shadow measurements). The summit of the western massif rises to 7.1 km above the plains to the south and west (*Schenk et al.* [2001] obtained a stereo measurement of 6.0 km and a limb profile measurement of 6.6 km) and the eastern mesa to 2.0 km above the plains to the south and east (*Schenk et al.* [2001] also obtained a stereo measurement of ~2.0 km). The floor of Tvashtar Paterae, which is surrounded by the massif and mesa, is elevated 0.8 km above the plains that surround the Tvashtar Paterae complex.

8. Conclusion

This paper describes our efforts to generate the most complete topographic map of Io to date using stereo analysis of both Voyager and Galileo imagery, with the individual DEMs being controlled using Galileo limb profiles [*Thomas et al.*, 1998]. We have mosaicked 70 stereo DEMs, ranging in resolution from 0.14 to >4 km/pixel, together to form the final DEM, which covers ~75% of Io's surface. This DEM presents an advantage over previous studies that have inferred Io's global shape using control point networks and limb profiles in that it represents a continuous topographic data set that allows precise identification of the amplitudes and lateral extents of long-wavelength variations in Io's topography.

Given the difficulty of applying stereo processing techniques to Io, we have experimented with and refined the relevant procedures in order to create what we consider to be the most reliable DEMs. We have assessed the stereo DEM's quality by quantifying topographic residuals between it and the Galileo limb profiles, which are the only directly measured relative heights for Io's topography, and find that a mean absolute residual of 0.61 km exists between the two data sets, with large absolute residuals reaching >1 km in magnitude generally being attributed to unsuppressed short-wavelength noise or off-limb topography remaining in certain parts of the stereo DEM and limb profiles. A few areas of laterally sustained high residuals reaching several hundreds of kilometers across are interpreted to result from anomalous topography within the limb profiles rather than the smoothing filter applied to the stereo DEM.

Concerning the global shape of Io, we have identified an arrangement of basins and swells in our DEM that, as far as can be determined due to limitations in coverage, extends from 80°W to 345°W in longitude and from 30°S to 55°N in latitude, and displays a longitudinal wavelength of 130° (roughly equivalent to a spectral degree of $l = 3$) and an amplitude reaching 1.5 km. This pattern is not the same as that identified by the Voyager-era control point network study of *Gaskell et al.* [1988], which is not apparent in our DEM. We have applied spherical harmonics analysis to the limb topography, expanding only to degree $l = 3$ in accordance with the wavelength of the DEM basins and swells, in order to investigate whether the same patterns manifest themselves using this alternative processing technique that, like the DEM, is ultimately controlled by the limb profiles. However, we find the spherical harmonics topography to present a very different pattern to that seen in the DEM, one that is much more latitudinally variable than longitudinally.

We have found that the locations of the basins correspond well to increased spatial densities of mountains and the swells to increased spatial densities of volcanic centers, as determined by *Kirchoff et al.* [2011], which stands as the most comprehensive study of the distributions of these landforms across Io. However, we acknowledge that the wavelength of the basins and swells in our DEM is best represented by a spectral degree ($l = 3$) that is different from that for which *Kirchoff et al.* [2011] found there to be the most significant power ($l = 2$), meaning that comparison between these two results is not strictly feasible. *Kirchoff et al.* [2011] found there to be minimal power and correlation at degree $l = 3$. Despite this, a very similar distribution of mountains and volcanoes to that apparent at the $l = 2$ degree has been identified by other studies including *Schenk et al.* [2001] and *Hamilton et al.* [2013] using independent methods to those of *Kirchoff et al.* [2011], and which therefore also correlate well to the locations of the basins and swells identified in our study. Given such correlation, we consider the basins and swells in our DEM to represent a significant contribution to understanding the distribution of heat flow across Io, which is intimately related to models for the location of tidal heating in its interior [*Tackley et al.*, 2001]. The coincidence of swells with concentrations of volcanic centers, and basins with mountain concentrations, supports the hypothesis that in lower areas, the compressional stresses associated with burial, subsidence, and compression of volcanic deposits predominate and mountain formation occurs preferentially over volcanism, while elevated areas are experiencing upwelling of asthenospheric material that creates extension which offsets the compressive regime, resulting in enhanced volcanic activity. The longitudinal rather than latitudinal dependence of both the basins/swells and mountain/volcano distributions indicates that heat flow distribution across the surface is also longitudinally dependent; this scenario is best described by the asthenospheric heating model of *Tackley et al.* [2001], which predicts high heat flow (and therefore upwelling, extension, and enhanced volcanism) at the sub-Jovian and anti-Jovian points on Io, and low heat flow (and therefore compression, reduced volcanism, and enhanced mountain building) at the leading and trailing points. The asthenospheric convection scenario would be expected to create relative differences in elevation between areas of extension and compression, but the slight eastward shift of both the basins/swells and volcano/mountain concentrations from these respective points is more consistent with the nonsynchronous rotation scenario, which does not specifically predict any elevation difference between the separate areas. *Hamilton et al.* [2013] discuss various alternatives to nonsynchronous rotation as a means for accounting for this offset, including lateral migration of upwelling magma and tides generated within a global partial melt layer modifying patterns of expected heat flux.

In addition to the global shape investigation, the stereo DEM also reveals topographic signatures of various regional-scale features, some of which are visible in Voyager and Galileo imagery, whereas others are more subtle. The global geological map of *Williams et al.* [2011] has assisted in our analyses of these features. These include an ~1000 km diameter, 2 km deep depression at 25°S, 135°W, the boundaries of which correlate well to a unit of undivided flow material mapped by *Williams et al.* [2011], and which may represent flows from an adjacent patera filling a preexisting topographic depression, or alternatively flows that have buried their source patera located at the nadir of the depression. A "topographic arc" comprising separate units of mountain and layered plains is identified at 42.5°S, 169.5°W, the mountainous portions of which display a fabric that potentially indicates a shared uplift origin as a consequence of a regional compressive regime. Prominent-named features that display topographic signatures include Loki Patera, which displays a depth of 2 km but has a topographic signature that is not confined to within the boundaries of Loki Patera in visible imagery, and the shield volcano Ra Patera, the positive topographic signature of which is emphasized by two smaller paterae on its south rim that show absent south rims in the DEM and imagery,

and long lava flows with negative topographic signatures stretching to the south. Tvashtar Paterae represents a rare example of high-resolution stereo data covering a complex of comparatively small-scale paterae, and the data are sufficient to allow us to define elevations for each of the separate geomorphological units of which the complex is composed.

Our study, building on the earlier work of *Schenk et al.* [1997, 2001, 2004], represents the broadest examination of Io's global- and local-scale topographies using stereo methods to date. The emphasis on refinement of these technique within this paper illustrates the great difficulty in applying it to Io, and while we consider the results of our investigation to represent a significant contribution to the Io literature, the quality of the data still remains inferior to corresponding stereo data sets obtained for the other Galilean satellites by Galileo and for the Saturnian satellites by Cassini. While we are confident that we have generated the most reliable stereo DEM of Io possible using the available techniques, there remains the issue of lack of agreement between the topography seen in our DEM and the results of earlier studies [e.g., *Gaskell et al.*, 1988; *Ross et al.*, 1990] that have used independent methods and different data sets to derive a global shape for Io, as well as the comprehensive volcano and mountain distribution study of *Kirchoff et al.* [2011]. This also includes our own processing of the limb profiles using spherical harmonics, which yields global topography patterns that do not correlate to what we see in the stereo DEM. *Oberst and Schuster* [2004] considered the large disparities between their control point shape model of Io and that of *Gaskell et al.* [1988] to stem from limitations of the control point network technique associated with small numbers of images and gaps in the coverage; the same limitations can also be said to apply to any attempt to infer topography from Voyager and Galileo imagery, including our stereo DEMs. We reiterate the assertion of *Oberst and Schuster* [2004] that Io researchers interested in global topographic maps must anticipate an Io orbiter with a dedicated photogrammetric camera or a laser altimeter on board, which would represent a considerable engineering challenge given the harsh radiation environment Io is located in. Until then, our stereo DEM, while not providing global coverage, stands as the most comprehensive continuous topographic data set of Io's surface.

Acknowledgments

The supporting data included with this paper consist of a cube file of the Io DEM (which can be viewed by downloading ISIS3 from the USGS website: http://isis.astrogeology.usgs.gov/Installation/) and 18 tiff files of the limb and stereo topographic profiles and ground tracks for the Galileo limb profiles used to control the DEM. The authors wish to thank Michelle Kirchoff, Peter Thomas, David Williams, and Ashley Davies for their comments, which helped to improve this paper. This research was supported by funding from the NASA Outer Planet Research Program, as well as the Lunar and Planetary Institute.

References

Anderson, J. D., R. A. Jacobsen, and E. L. Lau (2001), Io's gravity field and interior structure, *J. Geophys. Res.*, *106*, 32,963–32,969, doi:10.1029/2000JE001367.

Belton, M., et al. (1996), Galileo's first images of Jupiter and the Galilean satellites, *Science*, *274*, 377–385.

Bills, B. G., and A. J. Ferrari (1977), Harmonic analysis of lunar topography, *Icarus*, *31*, 244–259.

Bland, M. T., K. N. Singer, W. B. McKinnon, and P. M. Schenk (2012), Crater relaxation on Enceladus: Tales of high heat fluxes in unexpected places, Lunar Planet. Sci. XLIII, abstract #2168.

Carr, M. H., A. S. McEwen, K. A. Howard, F. C. Chuang, P. Thomas, P. Schuster, J. Oberst, G. Neukum, G. Schubert, and Galileo Imaging Team (1998), Mountains and calderas on Io: Possible implications for lithosphere structure and magma generation, *Icarus*, *135*, 146–165.

Davies, A. G. (2003), Temperature, age and crust thickness distributions of Loki Patera on Io from Galileo NIMS data: Implications for resurfacing mechanism, *Geophys. Res. Lett.*, *30*(21), 2133, doi:10.1029/2003GL018371.

Davies, A. G. (2007), *Volcanism on Io: A Comparison With Earth*, Cambridge Univ. Press, Cambridge, U. K.

Davies, M. E., and F. Y. Katayama (1981), Coordinates of features on the Galilean satellites, *J. Geophys. Res.*, *86*, 8635–8657, doi:10.1029/JA086iA10p08635.

Davies, M. E., et al. (1998), The control networks of the Galilean satellites and implications for global shape, *Icarus*, *135*, 372–376.

Gaskell, R. W., and S. P. Synnott (1987), Shape and topography of Io, *Bull. Am. Astron. Soc.*, *19*(3), 824.

Gaskell, R. W., S. P. Synnott, A. S. McEwen, and G. G. Schaber (1988), Large-scale topography of Io: Implications for internal structure and heat transfer, *Geophys. Res. Lett*, *15*, 581–584, doi:10.1029/GL015i006p00581.

Geissler, P., A. McEwen, C. Phillips, L. Keszthelyi, and J. Spencer (2004), Surface changes on Io during the Galileo mission, *Icarus*, *169*, 29–64, doi:10.1016/j.icarus.2003.09.024.

Greenberg, R., and S. J. Weidenshilling (1984), How fast do Galilean satellites spin?, *Icarus*, *58*, 186–196.

Hamilton, C. W., C. D. Beggan, S. Still, M. Beuthe, R. M. C. Lopes, D. A. Williams, J. Radebaugh, and W. Wright (2013), Spatial distribution of volcanoes on Io: Implications for tidal heating and magma ascent, *Earth Planet. Sci. Lett.*, *361*, 272–286, doi:10.1016/j.epsl.2012.10.032.

Howell, R. R., and R. M. C. Lopes (2007), The nature of the volcanic activity at Loki: Insights from Galileo NIMS and PPR data, *Icarus*, *186*, 448–461, doi:10.1016/j.icarus.2006.09.022.

Keszthelyi, L., et al. (2001), Imaging of volcanic activity on Jupiter's moon Io by Galileo during the Galileo Europa Mission and the Galileo Millennium Mission, *J. Geophys. Res.*, *106*, 33,025–33,052, doi:10.1029/2000JE001383.

Khurana, K. K., X. Jia, M. G. Kivelson, F. Nimmo, G. Schubert, and C. T. Russell (2011), Evidence of a global magma ocean in Io's interior, *Science*, *332*, 1186–1189, doi:10.1126/science.1201425.

Kirchoff, M. R., W. B. McKinnon, and P. M. Schenk (2011), Global distribution of volcanic centers and mountains on Io: Control by asthenospheric heating and implications for mountain formation, *Earth Planet. Sci. Lett.*, *301*, 22–30, doi:10.1016/j.epsl.2010.11.018.

Lopes-Gautier, R., et al. (1999), Active volcanism on Io: Global distribution and variations in activity, *Icarus*, *140*, 243–264.

Matson, D. L., A. G. Davies, G. J. Veeder, J. A. Rathbun, T. V. Johnson, and J. C. Castillo (2006), Io: Loki Patera as a magma sea, *J. Geophys. Res.*, *111*, E09002, doi:10.1029/2006JE002703.

McCauley, J. F., B. A. Smith, and L. A. Soderblom (1979), Erosional scarps on Io, *Nature*, *280*, 736–738.

McEwen, A. S., et al. (1998), Active volcanism on Io as seen by Galileo SSI, *Icarus*, *135*, 181–219.
McEwen, A. S., R. Lopes-Gautier, L. Keszthelyi, and S. W. Kieffer (2000a), Extreme volcanism on Jupiter's moon Io, in *Environmental Effects on Volcanic Eruptions: From Deep Oceans to Deep Space*, edited by J. R. Zimbelman and T. K. P. Gregg, pp. 179–205, Kluwer Acad., New York.
McEwen, A. S., et al. (2000b), Galileo at Io: Results from high-resolution imaging, *Science*, *288*, 1193–1198.
Milazzo, M., P. Geissler, R. Greenburg, L. Keszthelyi, A. McEwen, J. Radebaugh, and E. Turtle (2001), Non-synchronous rotation of Io?, Paper presented at Conference on Jupiter: Planet, satellites and magnetosphere, Univ. of Colorado, Boulder, Colo., June 25–30.
Moore, J. M., and P. M. Schenk (2007), Topography of endogenic features on Saturnian mid-sized satellites, Lunar Planet. Sci. XXXVIII, abstract #2136.
Moore, J. M., R. J. Sullivan, F. C. Chuang, J. W. Head, A. S. McEwen, M. P. Milazzo, B. E. Nixon, R. T. Pappalardo, P. M. Schenk, and E. P. Turtle (2001), Landform degradation and slope processes on Io: The Galileo view, *J. Geophys. Res.*, *106*, 33,223–33,240, doi:10.1029/2000JE001375.
Nimmo, F., B. G. Bills, P. C. Thomas, and S. W. Asmar (2010), Geophysical implications of the long-wavelength topography of Rhea, *J. Geophys. Res.*, *115*, E10008, doi:10.1029/2010JE003604.
Nimmo, F., B. G. Bills, and P. C. Thomas (2011), Geophysical implications of the long-wavelength topography of the Saturnian satellites, *J. Geophys. Res.*, *116*, E11001, doi:10.1029/2011JE003835.
Oberst, J., and P. Schuster (2004), Vertical control point network and global shape of Io, *J. Geophys. Res.*, *109*, E04003, doi:10.1029/2003JE002159.
Peale, S. J., P. Cassen, and R. T. Reynolds (1979), Melting of Io by tidal dissipation, *Science*, *203*, 892–894.
Phillips, C. B., N. P. Hammond, G. Robuchon, F. Nimmo, R. Beyer, and J. Roberts (2012), Stereo imaging, crater relaxation, and thermal histories of Rhea and Dione, Lunar Planet. Sci. XLIII, abstract #2571.
Radebaugh, J., L. P. Keszthelyi, A. S. McEwen, E. P. Turtle, W. Jaeger, and M. Milazzo (2001), Paterae on Io: A new type of volcanic caldera?, *J. Geophys. Res.*, *106*, 33,005–33,020, doi:10.1029/2000JE001406.
Rathbun, J. A., J. R. Spencer, and A. G. Davies (2002), Loki, Io: A periodic volcano, *Geophys. Res. Lett.*, *29*(10), 1443, doi:10.1029/2002GL014747.
Ross, M. N., and G. Schubert (1985), Tidally forced viscous heating in a partially molten Io, *Icarus*, *64*, 391–400.
Ross, M. N., G. Schubert, T. Spohn, and R. W. Gaskell (1990), Internal structure of Io and the global distribution of its topography, *Icarus*, *85*, 309–325.
Schenk, P. M. (2002), Thickness constraints on the icy shells of the Galilean satellites from a comparison of crater shapes, *Nature*, *417*, 419–421.
Schenk, P. M. (2010), *Atlas of the Galilean Satellites*, Cambridge Univ. Press, New York.
Schenk, P. M., and M. H. Bulmer (1998), Origins of mountains on Io by thrust faulting and large-scale mass movement, *Science*, *279*, 1514–1516.
Schenk, P. M., A. McEwen, A. G. Davies, T. Davenport, K. Jones, and B. Fessler (1997), Geology and topography of Ra Patera, Io, in the Voyager era: Prelude to eruption, *Geophys. Res. Lett.*, *24*, 2467–2470, doi:10.1029/97GL02688.
Schenk, P. M., H. Hargitai, R. Wilson, A. McEwen, and P. Thomas (2001), The mountains of Io: Global and geological perspectives from Voyager and Galileo, *J. Geophys. Res.*, *106*, 33,201–33,222, doi:10.1029/2000JE001408.
Schenk, P. M., R. R. Wilson, and A. G. Davies (2004), Shield volcano topography and the rheology of lava flows on Io, *Icarus*, *169*, 98–110, doi:10.1016/j.icarus.2004.01.015.
Schubert, G. T., T. Spohn, and R. T. Reynolds (1986), Thermal histories, compositions and internal structures of the moons of the solar system, in *Satellites*, edited by J. A. Burns and M. S. Matthews, pp. 224–292, Univ. of Arizona Press, Tucson.
Segatz, M., T. Spohn, M. N. Ross, and G. Schubert (1988), Tidal dissipation, surface heat flow, and figure of viscoelastic models of Io, *Icarus*, *75*, 187–206.
Smith, B. A., et al. (1979), The Jupiter system through the eyes of Voyager 1, *Science*, *204*, 951–972.
Spencer, J. R., et al. (2007), Io volcanism seen by new horizons: A major eruption of the Tvashtar volcano, *Science*, *318*, 240–243, doi:10.1126/science.1147621.
Synnott, S. P., J. E. Riedel, and R. W. Gaskell (1985), Shape of Io, *Bull. Am. Astron. Soc.*, *17*, 692.
Tackley, P. J. (2001), Convection in Io's asthenosphere: Redistribution of nonuniform tidal heating by mean flows, *J. Geophys. Res.*, *106*, 32,971–32,981, doi:10.1029/2000JE001411.
Tackley, P. J., G. Schubert, G. A. Glatzmaier, P. Schenk, J. T. Ratcliff, and J.-P. Matas (2001), Three-dimensional simulations of mantle convection in Io, *Icarus*, *149*, 79–93.
Thomas, P. C., et al. (1998), The shape of Io from Galileo limb measurements, *Icarus*, *135*, 175–180.
Turtle, E. P., et al. (2001), Mountains on Io: High-resolution Galileo observations, initial interpretations, and formation models, *J. Geophys. Res.*, *106*, 33,175–33,199, doi:10.1029/2000JE001354.
Turtle, E. P., et al. (2004), The final Galileo SSI observations of Io: Orbits G28-I33, *Icarus*, *169*, 3–28, doi:10.1016/j.icarus.2003.10.014.
Veeder, G. J., D. L. Matson, T. V. Johnson, D. L. Blaney, and J. D. Goguen (1994), Io's heat flow from infrared radiometry: 1983–1993, *J. Geophys. Res.*, *99*, 17,095–17,162, doi:10.1029/94JE00637.
Veeder, G. J., A. G. Davies, D. A. Williams, D. L. Matson, T. V. Johnson, and J. Radebaugh (2011), Io: Heat flow from dark paterae, *Icarus*, *212*, 236–261, doi:10.1016/j.icarus.2010.09.026.
Veeder, G. J., A. G. Davies, D. L. Matson, T. V. Johnson, D. A. Williams, and J. Radebaugh (2012), Io: Volcanic thermal sources and global heat flow, *Icarus*, *219*, 701–722, doi:10.1016/j.icarus.2012.04.004.
White, O. L., and P. M. Schenk (2014), Topographic mapping of paterae and layered plains on Io using photoclinometry, Lunar Planet. Sci. XLV, abstract #1540.
White, O. L., P. M. Schenk, and A. J. Dombard (2013), Impact basin relaxation on Rhea and Iapetus and relation to past flow, *Icarus*, *223*, 699–709, doi:10.1016/j.icarus.2013.01.013.
Williams, D. A., P. M. Schenk, J. M. Moore, L. P. Keszthelyi, E. P. Turtle, W. L. Jaeger, J. Radebaugh, M. P. Milazzo, R. M. C. Lopes, and R. Greeley (2004), Mapping of the Culann-Tohil region of Io from Galileo imaging data, *Icarus*, *169*, 80–97, doi:10.1016/j.icarus.2003.08.024.
Williams, D. A., L. P. Keszthelyi, D. A. Crown, J. A. Yff, W. L. Jaeger, P. M. Schenk, P. E. Geissler, and T. L. Becker (2011), Geologic map of Io: U.S. Geological Survey Scientific Investigations Map 3168, scale 1:15,000,000, 25 p.
Wilson, L., and J. W. Head (2001), Lava fountains from the 1999 Tvashtar Catenae fissure eruption on Io: Implications for dike emplacement mechanisms, eruption rates, and crustal structure, *J. Geophys. Res.*, *106*, 32,997–33,004, doi:10.1029/2000JE001323.